THE ROLE OF AEROSOLS IN NORTHERN TROPICAL ATLANTIC SEA

SURFACE TEMPERATURE ANOMALIES

by

Amato T. Evan

A dissertation submitted in partial fulfillment of

the requirements for the degree of

Doctor of Philosophy

(Atmospheric and Oceanic Sciences)

at the

UNIVERSITY OF WISCONSIN-MADISON

2009

UMI Number: 3367496

INFORMATION TO USERS

The quality of this reproduction is dependent upon the quality of the copy
submitted.   Broken or indistinct print, colored or poor quality illustrations
and photographs, print bleed-through, substandard margins, and improper
alignment can adversely affect reproduction.
In the unlikely event that the author did not send a complete manuscript
and there are missing pages, these will be noted.   Also, if unauthorized
copyright material had to be removed, a note will indicate the deletion.

UMI®

A dissertation entitled

The role of aerosols in northern tropical Atlantic sea surface temperature anomalies

submitted to the Graduate School of the
University of Wisconsin-Madison
in partial fulfillment of the requirements for the
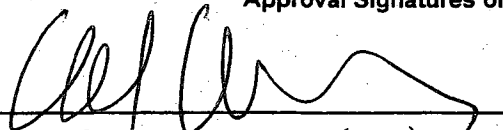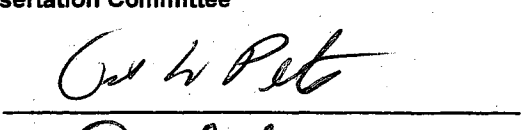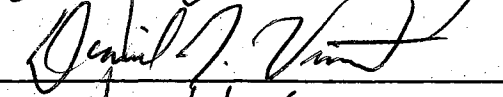degree of Doctor of Philosophy

by

Amato Tomas Evan

Date of Final Oral Examination: 27 April 2009

Month & Year Degree to be awarded: **December**   **May** 2009   **August**

****

Approval Signatures of Dissertation Committee
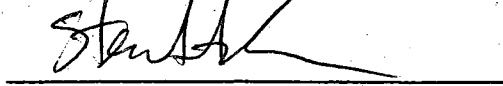
Signature, Dean of Graduate School

Martin Cadwallader   Aw.

Abstract

Observations and models demonstrate that northern tropical Atlantic sea surface temperatures are sensitive to regional changes in stratospheric volcanic and tropospheric mineral aerosols. However, it is unknown to what extent the temporal variability of these aerosols shapes observed Atlantic temperature anomalies on all time scales. Simultaneously, 26 years of daily retrievals of aerosol optical thickness from the Advanced Very High Resolution Radiometer suggest strong seasonal to decadal local variability in aerosol optical thickness. However, to-date no study has used the information from these satellites in order to answer the question of the role of aerosols in observed temperature anomalies.

The aim of this thesis is to develop a method for using satellite data in conjunction with simple models to estimate the ocean mixed layer response to aerosol forcing, and then to understand those estimates in terms of recent observed sea surface temperature variability. To do this I create a northern tropical Atlantic climatology of the aerosol direct effect by calculating the change in downwelling surface solar and longwave flux, based on monthly and one-half degree satellite retrievals of aerosol optical depth. I next use this forcing climatology to drive a simple mixed layer model to estimate the integrated ocean temperature response to the aerosol radiative forcing. The output of this mixed layer model is then directly compared to observations of sea surface temperature in order to quantify the role of aerosols in recent ocean temperature variability.

The results from this analysis suggest that low frequency changes in northern tropical Atlantic temperatures are largely the mixed layer response to regional variability in mineral and stratospheric aerosols, with 70% of the upward trend in observed temperatures being directly attributed to aerosol variability, and 67% of the five year smoothed variability around that upward trend also being attributed to local changes in aerosols. Consequently, my results also imply that direct effects from other forcings (e.g., increases in greenhouse gasses or salinity driven changes in the deep ocean circulation) constitute no more than 23% of the variance in the long-term temperature signal, and no more than 30% of the total upward trend.

Acknowledgements

I strongly believe that the work presented here has been a collaboration between myself and Professors Ralf Bennartz, Daniel Vimont, and Andrew Heidinger. Without the guidance and support of these three members of my PhD committee none of the ideas that motivated this study would have been realized, and certainly I would be much further away from completion of my dissertation. I would also like to thank the other members of my PhD committee for their direction and suggestions – Professors Steven Ackerman, Grant Petty, Jonathan Foley, and Jim Kossin. In addition, I owe a debt of gratitude to several others who have helped with various pieces of this project, including Professors Dave Turner, Galen McKinley, and Gunnar Myhre, Drs. Bryan Baum, Jeff Key, Sun Wong, and Hector Corrada-Bravo, and Val Bennington, Jean Philips, Dan Bull, Jason Dunion and Chris Velden.

I would also like to thank my wife, Paula, for being so supportive and motivating throughout this process, for translation work in the first chapter, and for "toughing-it-out" with me during this one last Wisconsin winter. And finally my son Joaquin, for sleeping through the night only two months into life, for not teething before my defense date, and for just being really cute little dude.

Table of Contents

List of Figures

List of Tables

1 Introduction

1.1 Thesis Outline

This thesis explores the role of aerosols in shaping recently observed ocean temperature anomalies of the northern tropical Atlantic using a combination of satellite retrievals of aerosols optical depth, long and shortwave radiative transfer models, and a simple stochastic mixed layer model. This work is organized in the following manner. Section 1.2 of this chapter contains a historical account of research into Atlantic dust outbreaks, spanning the time period of 1154 through 2009, and section 1.3 gives a more specific literature review of research into the radiative effects of dust on ocean surface temperatures.

The second chapter of this work focuses on the satellite retrievals of aerosol optical depth and using these data to estimate the aerosol direct effect. More specifically, Section 2.1 provides basic background information on the satellite data used and presents a climatology of dust and stratospheric aerosol optical depth over the northern tropical Atlantic. Section 2.2 describes the radiative transfer models used to estimate the aerosol direct effect, discusses the merits and weakness of the methods used. Section 2.3 provides a limited validation of the shortwave radiative transfer model by making comparisons to shipboard observations of downwelling solar flux in the Atlantic during several dust outbreaks. Lastly, section 2.4 presents a climatology of northern tropical Atlantic dust and stratospheric aerosol surface forcing based on the output of the radiative transfer models, which use the satellite observations of aerosol optical depth as input.

The third chapter focuses on the estimation of the ocean mixed layer response to aerosols. Section 3.1 describes the simple stochastic mixed layer model, the basis for the slightly more complicated one used here. Section 3.2 presents the concept of seasonal reemergence of ocean temperature anomalies, describing and validating the mixed layer model I use, which is shown to be able to reproduce the temporal pattern of persistence in sea surface temperature variability. Section 3.3 describes the method in which I force this mixed layer model with my estimates of the aerosol direct effect, detailing the various model runs. At the end of this section I present a climatology of the northern tropical Atlantic mixed layer temperature response to dust, volcanic stratospheric aerosols, and then both dust and the volcanic aerosols, analyzing the spatial and temporal variability of each.

The fourth chapter makes a detailed comparison of observed sea surface temperature anomalies with output from the mixed layer model, in the northern tropical Atlantic, and over the time period of 1982–2008. Section 4.1 briefly describes the spatial and temporal variability of observed sea surface temperature anomalies. Section 4.2 presents the conceptual framework for which model output will be compared with observations. Following this, I quantify the importance of dust, stratospheric volcanic aerosols, and both dust and the volcanic aerosol jointly, in shaping upward trends in observed temperature variability, and influencing the variability about those trends. This analysis is presented both in terms of temporal, and spatial sea surface temperature variability.

Chapter Five is devoted to analysis of sensitivity in the methods used for estimating the ocean mixed layer's temperature response to aerosols. Here I use reasonable estimates of uncertainty in various model parameters to test the sensitivity of the mixed layer model output, and the comparisons with observations, to those uncertainties. Finally, in Chapter Six I summarize the work presented in this thesis, and my main findings, discussing their relevance to understanding the climate of this region and suggesting future work that is needed.

1.2 Early History of Atlantic Dust Storm Research

The earliest account of an African dust storm over the waters of the Atlantic Ocean has been attributed to the 12th century Arab geographer Muhammad al-Idrisi (1099-1166) (Radczewski 1839; Tchihatchef 1883; Game 1964; Ward 1914; Stuut et al. 2005). Al-Idrisi was commissioned in the 12th century by King Roger of Sicily to create a map of the known world. The account of his travels was later published in 1154 as *The Book of Roger*, and of the many maps he created, his map of the known world, which included Europe, North Africa, and Central Asia and was subdivided into a 7x10 grid (Figure 1.1), was the most accurate for the following several hundred years.

The Book of Roger has only in its entirety been translated from the original Arabic once; into French in 1838 (Idrisi and Jaubert 1836). Several passages within this translation refer to the Atlantic Ocean, particularly off the coast of West Africa, as the *Mer Ténébreuse*, or *Sea of Darkness*. While I have found this phrase in the first sections of the second, third, and sixth climates, The most descriptive entry related to the *Sea of*

Darkness is contained within the section that considers the southern half of the Iberian Peninsula (the first section of the fourth climate),

> *"Cette première section commence à la partie de l'extrême occident baignée par l'océan Ténébreux dont émane la mer de Syrie (la Méditerranée), qui s'étend vers l'orient. C'est là qu'est situé le pays Andalos, que les chrétiens appellent Espagne ou presqu'île d'Andalous, attendu que sa forme triangulaire se rétrécit du côté de l'orient au point de ne laisser entre la Méditerranée et l'Océan, qui l'entourent, qu'un intervalle de 5 journées. La plus grande largeur de cette presqu'île est d'environ 17 journées, à partir d'un cap de l'extrême occident où se termine la portion habitée de la terre ceinte par la mer Océane. Personne ne sait ce qui existe au delà de cette mer, personne n'a pu rien en apprendre de certain, à cause des difficultés qu'opposent à la navigation la profondeur des ténèbres, la hauteur des vagues, la fréquence des tempêtes, la multiplicité des animaux monstrueux et la violence des vents. Il y a cependant dans cet Océan un grand nombre d'îles, soit habitées, soit désertes; mais aucun navigateur ne se hasarde à le traverser ni à gagner la haute mer; on se borne à côtoyer, sans perdre de vue les rivages. Les vagues de cette mer, hautes comme des montagnes bien qu'elles s'agitent et se pressent, restent cependant entières et ne se brisent (littér. ne se fendent) pas. S'il en était autrement, il serait impossible de les franchir.*
> *"*

> *"This first section of the fourth climate begins at the western extreme, washed by the ocean of Darkness, from which the Syrian sea (the Mediterranean) emanates, which stretches towards the east. It is there where the country of Al-Andaluz resides, which Christians call Spain (Ichbâniyâ) or peninsula (djazîra) of Al-Andaluz, considering its triangular shape, which narrows on the east side to the extent of not leaving more than an interval of five days between the Mediterranean sea and the ocean that surrounds it. The widest side of this peninsula, about the size of seventeen days, from a cape situated on the western extreme, where the inhabited portion of the earth, surrounded by the sea of Darkness, ends. Nobody knows what exists beyond this sea, nobody has ever known anything for certain, because of the difficulties to navigation presented by the depth of darkness, the height of the waves, the frequency of tempests, the multiplicity of monstrous animals and the violence of the winds. There is, however, a good number of islands, inhabited or deserted, in this ocean; but no sailor ventures to traverse it, nor gain the high seas; instead they limit themselves to navigate alongside the coast, without loosing sight of the shores. The waves of this sea, as high as mountains, even if they shake and clash, remain intact and do not break. If they would break, it would be impossible to traverse them."*

In Arabic *Mer Ténébreuse* (*Mare Tenebrosum* in Latin and *Sea of Darkness* in English) is *Bahr al-Zulamat.*, and it has been suggested that the term *al-zulumat* may be referring to a passage of the Qur'aan that describes the state of an unbeliever as being like, *"the depths of darkness in a vast deep ocean, overwhelmed with billows, topped by billows, topped by [dark] clouds - depths of darkness, one above the other"* (Lunde 1992). It is more likely that the use of the word *darkness* by Al-Idrisi signified the unknown that lay beyond the western coast of Africa and Europe.

The first unambiguous account of an African dust outbreak over the Atlantic Ocean appearing in the scientific literature was in the 1721 proceedings of the French Academy of Sciences by P. Feuillée, *Observation sur une pluie de sable dans la mer Atlantique précedée d'une aurore boréale* (Observation on a sand rain in the Atlantic Ocean preceding an aurora borealis) (Feuillée 1721). This brief account describes the encounter of a ship with a "sand rain" on the 6th of April, 1719 at 45°N and 38°W, which lasted three hours.

During the dry season, coastal West Africa experiences strong surface trade winds from the N to NE. These dry and oftentimes dusty winds are known as the Harmattan winds, based on the Fante[1] name for this wind, *Aherramanta* (Thomson 1849) or *Aherramantah* (Dobson and Fothergill 1781), which refers to the season in which it is active. Dr. James Lind of the Royal English Navy, famous his discovery of the cure for scurvy, describes the Harmattan wind in *An essay on the most effectual means of preserving the health of seamen in the Royal Navy* (Lind 1762). Lind had observed the

---

[1] An ethnic group found in present day Ghana

Harmattan from several locations along the West African coast: Guinea, Guinea-Bissau, and Benin. At this time in history medical research was concerned with environmental factors that impacted health, specifically winds. This probably explains Dr. Lind's commentary, which begins, *"But of all vapours which infect the torrid zone, the most malignant and fatal are the Harmattans..."* Much Dr. Lind's description focuses on health risks attributed to the Harmattan, and anecdotal stories of deaths attributed to the wind. Lind also describes the Harmattan as occurring in the months of December through February, being southeasterly or northeasterly, changing the coastal ocean currents, and reducing visibility to less than 15 yards. The description of a northeasterly, dust-laden surface wind during the boreal winter months perfectly matches the modern-day definition of the Harmattan. Furthermore, Lind describes strong interannual variability in the Harmattan, a topic I explore in Chapter 2.

The theme of Dr. Lind's account of the Harmattan is describing its dangers to human health and mitigating actions one may take to avoid exposure. His ultimate suggestion for remedy, if you find yourself in the midst of a particularly "noxious" Harmattan, is to light a fire from wood fuel. However, it is not clear if the afflicted is to breath in the smoke, as an alternative to breathing dust particles, or if the draft initiated by the smoke clears the surrounding air. It is interesting to note, in the context of Lind's medical concerns related to the Harmattan, that modern research has made links between dust storms and increased incidence of human exposure to fungi, bacteria, virus-like microbial species (Gorbushina et al. 2007), silicosis, and asthma.

In 1780 J. P. Schottee published observations of the weather from 1775 through 1779 at the costal island of St. Lewis in Senegal (16°N & 16°W), with a detailed account of the temperature, wind direction, and general conditions from August 1778 through January 1779 (Schotte and Banks 1780). Like Lind, Schotte also focuses on the health effects of environmental conditions (e.g., heavy precipitation events, wind, air quality). However, Schotte's account of the Harmattan is unique; he notes that during the months of February through June, easterly winds often appear hazy and are associated with warm temperature anomalies. Schotte speculates that intense solar heating in the interior of the continent intensifies the easterly winds, which then mobilize dust into the atmosphere. Schotte provides an account of a dust storm over the Gambia River and noted the difference in color between the local soils and the suspended dust, which decreased visibility to 20 yards. Schotte also provides an account of being onboard a ship during a dust outbreak,

> *"The same thing I observed at sea from on board of a vessel in the month of March 1885, at the distance of about for or five leagues from the land near the latitude of Senegal. The wind having blown East in the night, I found in the morning the sails, shrouds, and deck, covered with an impalpable dust."*

Schotte continues by providing anecdotal evidence suggesting that the Harmattan is accompanied by a very dry air mass, including description of a method for cooling water used by the local indigenous population during the dry-air outbreaks[2]. Schotte does not concur with the observations of Lind, that the Harmattan poses a serious health risk.

---

[2] This consisted of placing water in a leather container, which is then hung from a tree. As the dry air encounters the leather pouch, which has become saturated, water on the

The British author Robert Norris traveled throughout West Africa in the late 18th century and encountered Harmattan outbreaks on several occasions. An account of these experiences, along with a commentary on the nature of the Harmattan, were published in 1781 by Matthew Dobson (Dobson and Fothergill 1781). Norris also published his account of the Harmattan in 1791 (Norris 1789), but only in terms of describing how these dry dust outbreaks affected local populations. Dobson's publication notes the reduction of visibility associated with the Harmattan, but does not make an explicit connection between dust particles as being the source of the haze. Dobson may have been one of the first to measure evaporation (Dobson 1775) using an evaporation pan, of 12 inches in diameter. Such a pan was given to Norris by Dobson particularly for the purpose of measuring evaporation during a Harmattan, who found that the Harmattan increasing evaporation by ½ to one tenth of an inch. Dobson inferred that, based on evaporation amounts and concurrent temperatures, that the annual Harmattan evaporation would be 133 inches.

Dobson also investigates the source of the Harmattan using measurements of wind direction taken at three locations during Harmattan outbreaks: easterly at Cape Verde (16°N & 23°W), northeasterly at present day Ghana (5°N & 0°E), and northerly at Cape Lopez (0°N & 8°W). Dobson makes a simple back trajectory and interprets that the point where all three lines converge is a possible source region for the Harmattan, 15°N & 25°E, present day Sudan. However, a simple triangulation with modern maps would

---

outer surface of the pouch evaporates, cooling the leather and subsequently the water contained within.

put the source region in northern Niger, an area where dust storms are known to originate from (Engelstaedter et al. 2006).

In 1833 during Darwin's voyage on the HMS Beagle, the ship encountered an African dust outbreak on the 16th of January near the Cape Verde islands (Darwin 1846). Darwin noted a fine reddish brown dust adhering to a wind vane on the mast of the ship, apparently filtered from the air by the sails, and observed that during his three week stay at the Cape Verde islands the wind was northeasterly and continually hazy, with constant precipitation of the fine dust particles. While Darwin was concerned with microscopic organisms contained within the dust, he also presents the first climatology of African dust storm activity over the Atlantic. This climatology was compiled from observations of dust falling on ship in the Atlantic, sometimes from personal communications. For example, R. B. James, who encountered a dust storm onboard the HMS Spey in March 1838 at 21N and 22W, sent to Charles Lyell, Darwin's colleague and mentor, dust samples collected from the ship and the results of several measurements made on the particles, including a borax test, the results of which suggested the presence of Iron (James 1838). While Darwin does not mention the results of the Borax test in this article, he does relate that Lyell found particles of different colors and irregular shapes, measuring about 1/1000th of a square inch.

Darwin's Atlantic dust climatology is largely based on published accounts, found in diaries, scientific journals, and captain's logs (e.g., Hayward (1839), Figure 1.2), of ships encountering dust storms. From these accounts he makes several observations about the nature of Atlantic dust outbreaks. Firstly, based on the northernmost

observation of a ship encountering a dust storm, or in this case the appearance of the remnants of a dust storm evidenced by discolored water, which is 28°N, and the southernmost observation of precipitating mineral aerosols, 10°N, Darwin concludes that dust outbreaks from Africa can span about 1600 miles of latitude. Secondly, based on the westernmost observation of suspended dust, which is at 35°W at a latitude roughly matching Cape Verde, the storms can also span 1030 miles of longitude. Thirdly, that all encounters with a dust storms occur when the wind direction is northeasterly or southeasterly. And lastly, that the season of these storms is January through April. Recently, dust samples that were taken by Darwin while onboard the *Beagle*, were analyzed and found to contain cultivable bacteria and fungi (Gorbushina et al. 2007).

The textbook *Introduction to Meteorology* (Thomson 1849) gives an excellent summary of various types of dust storms. Although the text does focus on over land dust storm activity, there is a brief description of the Harmattan. Here the Harmattan is described as a dry and dust laden wind blowing from the interior of West Africa and out over the Atlantic, primarily during the months of December through February, has a duration of three to 15 days, and occurs three or four times in a season (I note that the source of the information is not clear). Thomson also notes the following report of an encounter with the Harmattan while at sea.

> *"Jackson, in N. lat. 30°, and long. 10° 30', collected when twenty leagues from land, a wine-glassful of sand which had fallen upon deck after having been borne on the wind from Africa."*

Several other accounts of dust over the Atlantic are published second half of the 19th century (Ehrenberg 1863; Tchihatchef 1883). However, most notable among these is

a paper by Hellman (1878) who published what was at that time the most detailed climatology of Atlantic dust storm activity, based on ship observations. This work also included the first published map the locations of the ships' encounters with the dust, and wind barbs describing the wind direction at the time of the event. The ship observations extend well into the northern tropical Atlantic basin, and are all consistent with dust outbreaks being advected with the trade flow (Figure 1.3). It is interesting to note that until 1913 *Hellman* hypothesized that the dust had its origins in South America, mainly based on the disconnect between the color of the dust (reddish) and what *Hellman* believed to be the color of sand from the Sahara (white), and an erroneous belief that the prevailing winds over the northern tropical Atlantic were westerly (Ward 1914).

As science entered the modern era, study of dust storms over the Atlantic also focused on the composition of the aerosols (Radczewski 1839; Game 1964). However, nothing served to further understanding of the meteorology Atlantic dust storms more than 1) the dawn of the era of meteorological satellites (Prospero et al. 1970) and 2) the creation of an aerosol sampling station at the easternmost edge of the Caribbean (Delany et al. 1967). Prospero et al. (1970) use both data from the dust sampling site in Barbados and satellite imagery to make a detailed study of a dust outbreak occurring in June 1967. This paper is of special note since it is the first to provide direct and conclusive evidence for theories of Atlantic dust transport that had been proposed over the last 300 years. Since then scientific publications related to Atlantic dust outbreaks have increased exponentially (Kaufman et al. 2005b; Stout et al. 2009), and there exist several excellent review papers covering this period of time (e.g., Engelstaedter et al. (2006)).

1.3 Investigation of dust cooling the Atlantic

Miller and Tegen (1998) coupled an atmospheric general circulation model that included a seasonal cycle of global dust to a slab ocean in order to determine the coupled ocean atmosphere response to mineral aerosols. Their results suggested that dust does not strongly impact the surface radiation budget of SST across the northern tropical Atlantic. However, they also concede that the offline tracer-transport model used to generate dust loadings underestimate the westward extent of mineral aerosols from West Africa. Miller (2004) used an improved model for the simulation of Atlantic dust cover to show strong negative radiative forcing due to the presence of dust.

Yoshioka et al. (2007) used the NCAR CCSM ATM model with prognostic dust to investigate the climate response to mineral aerosols. The dust optical properties of Yoshioka et al. (2007) differ from those in Miller et al. (2004) in that the dust is less absorbing in the shortwave, consistent with findings of Highwood (Highwood et al. 2003) and Myhre et al. (2003), and therefore the output from their modeling study showed a strong dust surface forcing across the northern tropical Atlantic, with values here on the order of $-10 Wm^2$. Furthermore, this forcing resulted in a tropical North Atlantic cooling of SST that is on the order of $-0.5°C$.

More recently satellite data has been employed to provide empirical evidence for this effect. Scholaert and Merril (1998) showed that dust could have a non-negligible impact of local SST by modeling the instantaneous change in mixed layer temperatures due to dust, and off the coast of West Africa, by using satellite retrievals of aerosol optical thickness (AOT) in conjunction with a simple parameterization for the all-sky

forcing as a function of AOT. Lau and Kim (2007a; 2007b) demonstrated a lagged correlation between microwave SST and a satellite-based aerosol index (OMI) over the western half of the tropical northern Atlantic, with dust leading SST, for the month of July during 2005 and 2006. Evan (2007) argued that the 1.2K cooling, between 2005 and 2006, purported to be due to the increases in dust by Lau and Kim was an order of magnitude too large.

Foltz and McPhaden (2008a) used a multidecadal aerosol optical thickness time series from TOMS to show a strong correlation between AOT and changes in northern tropical Atlantic SST, suggesting that 35% of the interannual variability in SST is related to changes in dust cover. Evan et al. (2008) forced a shortwave radiative transfer model with 25 years of AOT estimates from the AVHRR to demonstrate that at least 33% of the recent upward trend in eastern tropical North Atlantic SST was forced by the downward trend in local dust cover over the same time. Foltz and McPhaden (2008b) again used AOT data from TOMS and a parameterized dust forcing efficiency to show that if let unbalanced, the decrease in dust cover over the last 25 years would result in a 3°C increase in the temperature of the mixed layer.

While these observational studies are instructive, none provide a thorough treatment of both the radiative perturbations due to dust and stratospheric aerosols associated with major volcanic events, and the integrated ocean mixed layer response to that forcing. Therefore, the question of how important local changes in aerosols are in shaping observed northern tropical Atlantic SST remain unanswered.

1.4 Figures

Figure 1.1 The Tabula Rogeriana (Roger's Map) of Muhammad al-Idrisi (1154).
Note the orientation of the roman numerals on the image (previous page), suggesting a
south-to-north vertical orientation and a east to west horizontal one. Image downloaded
at http://upload.wikimedia.org/wikipedia/commons/d/d3/TabulaRogeriana.jpg, and last
accessed on March 6, 2009.

DUST AT SEA. Extract from the Journal of Cap. J. W. Hayward, of the Brig Garland.

1839.	WIND.	WEATHER.	LAT.	LON.	REMARKS.
Feb. 9th	E.N.E.	Fine	10·0°	29·59°	The air during these five days has been full of a fine dust of a red colour which has lodged on our sails and rigging making every thing appear rusty. The nearest land, Cape Verd Islands, on the 9th, distant 450 miles; and on the 14th 850 miles.
10th	N.E. b E.	Ditto	7·57	28·10	
11th	N.E.	Ditto	5·48	27·11	
12th	N.E.	Hazy	4·25	26·30	
13th	N.E.	Hazy & Fine	2·56	26·30	

Figure 1.2 Account of ship's encounter with the Harmattan. Copy of the published account from Capt. J. W. Hayward, of the ship Brig Garland encountering a dust storm while in the northern tropical Atlantic during February 1839. Reprinted from Hayward (1839).

QuickTime™ and a
decompressor
are needed to see this picture.

Figure 1.3 Climatology of the Harmattan based on ship observations. Map of ships' observations of dust storms including wind directions, reprinted from Hellman (1878).

2 Aerosol Surface Forcing

2.1 Satellite based estimates of Atlantic dust cover

My nearly 30-year record of monthly dust storm activity is derived from aerosol optical thickness (AOT) retrievals made by the long-term Advanced Very High Resolution Radiometer (AVHRR) (Stowe et al. 1997). AVHRR 5-channel imagers have flown on the National Oceanographic and Atmospheric Administration series polar orbiting satellites since October of 1981 and provide one to three daily daytime observations of nearly every point on the globe at a 4km nadir resolution. AVHRR satellite processing is done within the Pathfinder Atmospheres Extended (PATMOSx) project[3], the follow on to the original Pathfinder Atmospheres effort (Jacobowitz et al. 2003). It is common that cloud detection algorithms misclassify optically thick dust storms as meteorological clouds, leading to AOT statistics that do not include the strongest storms (Evan et al. 2006). However, implementation of a dust detection algorithm within PATMOSx does increase accuracy of monthly mean AOT statistics, and direct comparisons to dust optical depth data from the Aerosol Robotic Network at costal sites shows excellent agreement (Evan et al. 2006).

I derive a dust optical thickness product in a manner similar to that of Evan et al., (2008), with some modest improvements. Starting with monthly mean AOT values (Stowe et al. 1997), I subtract estimations of stratospheric aerosols associated with volcanic eruptions (Sato et al. 1993) in order to create a data set of AOT that is not influenced by stratospheric H_2SO_4 associated with the eruptions of Mt. Pinatubo and El

---

[3] PATMOSx data are available at http://cimss.ssec.wisc.edu/patmosx/.

Chichón[4]. Although H_2SO_4 levels are persistent throughout the record, their levels are generally not high enough to have a radiative impact in my analysis. Since long-lived H_2SO_4 associated with these major eruptions is found within the stratosphere, I refer to the aerosol optical depth of these aerosols as the stratospheric aerosol optical depth (SAOD). Next, I remove from this processed AOT data an estimation of the sea salt contribution to the total aerosol signal (0.05) (Kaufman et al. 2005b). Finally, using a monthly climatology of dust fraction from the AVHRR dust detection algorithm (Evan et al. 2006), I set to zero any residual AOT values in regions where I did not detect the presence of mineral aerosols. This final step is useful in removing the impact of either anthropogenic aerosols, or aerosols associated with biomass burning (Johnson et al. 2008a; Johnson et al. 2008b), from my analysis. I consider the remaining AOT values to be a dust aerosol optical depth (DAOD). In regions where there is a mix of both smoke from biomass burning and dust, it is possible that my DAOD values may be too liberal. However, this mix of both dust and smoke is generally found over the Gulf of Guinea during the boreal winter months (Husar et al. 1997; de Graaf et al. 2006; Evan et al. 2006), which is outside the region of my analysis.

Figure 2.1 is a climatological map of this AVHRR satellite derived DAOD for the period of 1982–2007. Here, the highest DAOD values are found off the coast of West Africa, largely between the latitudes of 10°-20°N, and extending Westward to roughly 30°W longitude. Additionally, DAOD values greater than 0.1 are found from 0°-30°N

---

[4] stratospheric aerosol optical depth data are available at
http://data.giss.nasa.gov/modelforce/strataer/.

and 15°W to nearly 60°W. This spatial pattern of dust strongly reflects the boreal summertime activity, the peak season of dust storms activity, and essentially follows the trade flow across the tropical Atlantic. This picture of climatological DAOD appears to agree well with recent model-based estimated (Yoshioka et al. 2007), although DAOD values from the model appear to be slightly larger my satellite-based estimates.

A time series of dust optical depth (Figure 2.2) shows that monthly mean DAOD values have ranged from more than 0.3 to nearly 0 from 1982–2007. Peaks in activity occur in 1984, 1985, and 1991, while monthly minimums are seen in 1994 and 1995. It is possible that the minimums during these years are related to satellite artefacts, namely a reduction in the number of retrievals owing to higher solar zenith angles associated with satellite drift. However, setting these two minimum values to missing and replacing them with climatological values does not noticeably change my final results. The seasonal cycle in for tropical North Atlantic dust cover is nearly bi-modal (Figure 2.3), with the maximum in dust cover during June–July, and a smaller relative maximum during March. The minimum in activity occurs in November, with a less pronounced relative minimum in May. The grey crosses in Figure 2.3 represent all dust values recorded during the month, and the error bars are the standard error of the estimations of the climatological means (Preston 1991), calculated by dividing the standard deviation of the monthly values by the square root of one minus the number of monthly values. The monthly values in Figure 2.3 demonstrate that summertime dust loadings are not always stronger than wintertime values, although statistically speaking the error bars for June and July suggest that the summer months being the climatological maximum of dust activity is

robust. Furthermore, the minimum in activity seen during October–December appears to be persistent throughout my record.

In order to explore the interannual variability in tropical North Atlantic dust cover I smoothed the monthly dust time series with two recursive 13-month running mean filters (Figure 2.2). Here, maximums and minimums in dust activity occurred around 1985 and 2005, which are superimposed over a general downward trend in dust cover over the record. Although to-date no study has explicitly assigned causality to this interannual variability in Atlantic dust cover, it has been shown that during both the summer (Prospero and Lamb 2003) and winter seasons (Evan et al. 2006) year-to-year changes in dust cover are related to variations in previous-year Sahelian precipitation, and that wintertime dust production is strongly related to the strength of the North Atlantic Oscillation (Moulin et al. 1997), and to a lesser extent the El Niño / Southern Oscillation (Evan et al. 2006). The grey line in Figure 2.2 is of stratospheric aerosols (Sato et al. 1993) resulting from the eruptions of El Chichón in 1982, and Mt. Pinatubo in 1991.

2.2 Calculation of the Aerosol Surface Forcing

Spectrally resolved values of the dust and H_2SO_4 single scatter albedo, asymmetry parameter, and extinction coefficient across the solar and longwave parts of the spectrum are needed in order to estimate aerosol surface radiative forcing with satellite retrievals of optical thickness. Although mineral aerosol optical properties vary strongly from one source region to another, I use estimations of dust optical properties that have been generated from aerosol observations off the coast of West Africa (Myhre et al. 2003), and optical properties for sulfuric acid are from the AEROMIE model (Tsay and Stephens

1990), including single scatter albedo, asymmetry parameter, and coefficients of extinction, where the extinction is scaled to have a maximum value of one (Figure 2.4).

Light extinction by dust is dominated by forward scattering in the solar and absorption in the longwave, but extinction in the solar part of the spectrum is an order of magnitude stronger than that in the longwave (Figure 2.4), and light extinction by H_2SO_4 is dominated by scattering (Figure 2.4). Although the single scatter albedo of H_2SO_4 falls off unity at wavelengths greater than one micron, here the extinction coefficient is more than two orders of magnitude weaker than it is at, for example, 200nm (Figure 2.4). Considering that in my analysis the optical depth of stratospheric aerosols is never greater than 0.3, I treat these aerosols as purely scattering in this analysis, (e.g., I do not consider possible absorption of solar or longwave radiation).

To calculate the aerosol surface solar forcing I use a two-stream radiative transfer model (Meador and Weaver 1980) resolved at the nanometer scale to determine solar radiation at all solar zenith angles for any combination of dust and stratospheric aerosol loadings. Dust and stratospheric aerosol optical depths, which are available for one solar wavelength only, are extended across the solar spectrum by linearly scaling the retrieved values using their respective coefficients of extinction (Figure 2.4). Mineral and stratospheric aerosol optical properties are all transformed with delta scaling in order to better model forward scattering (Joseph et al. 1976).

With regard to solar radiation, I model the atmosphere as containing a well mixed absorbing CO_2 and O_2 layer, a stratospheric O_3 layer, tropospheric and stratospheric aerosol layers, and a Rayleigh layer that both absorbs and scatters solar radiation. For

simplicity of calculation I combine the optical properties of the stratospheric aerosol and Rayleigh layers, where the combined optical depth is the sum of the Rayleigh and stratospheric optical depths, and the combined single scatter albedo and asymmetry parameters are an average of the Rayleigh and stratospheric properties, weighted by their respective scattering optical depths. I allow for multiple scattering within each of these layers, and scattering between the tropospheric aerosol and a combined Rayleigh and stratospheric aerosol layer. I assume there is no multiple scattering between the gas, ozone, and water vapor layers.

Transmittance from the top of the atmosphere to the surface is obtained by summing the total diffuse and direct transmittance. Direct transmittance is defined as

$$ t_{dir} = \prod_i e^{-\frac{\tau_i}{\mu}}, \qquad (2.1) $$

where μ is the cosine of the solar zenith angle, τ is optical depth, and the subscript i refers to τ for 1) a well mixed gas, 2) ozone, 3) tropospheric aerosols (in this case dust), 4) water vapor, and 5) combined Rayleigh and stratospheric aerosols. Diffuse transmittance is approximated as the product of the direct transmittance through the well-mixed gas and ozone, diffuse water vapor transmittance, and multiple scattering between the tropospheric aerosol and combined Rayleigh and stratospheric aerosol layers. Monthly climatological values of water vapor are from the NCEP reanalysis (Kalnay et al. 1996)[5].

Cloud-free sky aerosol forcing is determined by subtracting surface clear-sky (no aerosols) solar radiation values from those calculated with non-zero values of mineral,

---

[5] NCEP Reanalysis data available at
http://www.cdc.noaa.gov/data/reanalysis/reanalysis.shtml.

stratospheric, or mineral and stratospheric aerosol optical thickness. Figure 2.5 contains plots of the surface forcing as a function of μ (cosine of the solar zenith angle) for various dust and stratospheric aerosol optical depths. In the dust case, even at an optical depth of 0.2, the surface forcing is 10 to 30W/m^2 for μ values greater than 0.1, corresponding to a solar zenith angle of about 84°. Although monthly mean values of dust optical thickness of 1.0 and higher are not a frequent feature of the tropical North Atlantic, they are not uncommon near the coast of West Africa. In these cases, at values of μ equal to one (corresponding to the sun being directly overhead), the surface forcing is very strong, ranging from 100 to 400W/m^2. Stratospheric aerosol amounts over the tropical North Atlantic do not exceed values of 0.3 (Sato et al. 1993), but per unit optical thickness H_2SO_4 has a stronger radiative impact than does dust. For example, for an optical thickness of 0.2 at μ equal to one, the dust surface forcing is about 25W/m^2 and the sulfuric acid forcing is almost double that at 40W/m^2. Additionally, in my analysis dust and stratospheric optical depth values range from 0.0 to 3.0 and 0.0 to 0.3, respectively. Over these ranges of values the combined surface forcing from the two aerosol types is roughly linear, except at extremely high solar zenith angles, where surface forcing per unit dust optical depth is stronger than low stratospheric optical depth values (Figure 2.6).

One validation of this simple two-stream model is made by comparing my forcing values with those generated by STREAMER[6] (Key and Schweiger 1998). Contour plots of forcing as a function of μ and DAOD for my model and STREAMER, and with SAOD equal to zero (Figure 2.7) and 0.2 (Figure 2.8), show very similar results, with the

---

[6] STREAMER can be downloaded at http://stratus.ssec.wisc.edu/streamer/streamer.html.

difference between the two in both cases being negligible for DAOD values below 0.5. At high values of μ and DAOD the forcing calculations from STREAMER are on the order of 10 W/m^2 higher than ours, with maximums in the differences of about 25 W/m^2. The plots in Figure 2.7 and Figure 2.8 suggest that my forcing calculations may be conservative, but it is also possible that the STREAMER values are too strong, especially since my simple model has a more that 100 times higher spectral resolution than does STREAMER. These differences are considered further in the next section of this chapter, when comparisons of the shortwave models to observation are made.

Longwave dust radiative transfer calculations are performed solely within STREAMER (Key and Schweiger 1998). In general dust longwave forcing is an order of magnitude weaker than that in the shortwave; for a dust optical depth of 3.0 the solar forcing can be as high as 400W/m^2 (Figure 2.5), while the longwave forcing is just under 12W/m^2 (Figure 2.9). It is worth noting that, at least during the summer months, Atlantic dust outbreaks are accompanied by a mid-layer dry air anomaly. Recently *Dunion et al.* (Dunion and Marron 2008) demonstrated that the atmospheric profiles of temperature and humidity across the tropical North Atlantic and Caribbean were bimodal; a moist tropical environment, and a more stable and dry one associated with African dust outbreaks. The reduced column water vapor during the dust, or Saharan Air Layer (SAL), outbreaks will also alter surface radiation budgets (Figure 2.10).

I calculate the water vapor forcing of the SAL by subtracting an estimate of the surface longwave+shortwave radiation for a typical SAL moisture and temperature profile minus that for a moist non-SAL profile (Dunion and Marron 2008). I also

calculate the surface forcing for a "½ SAL" case, where the moisture and temperature profiles are taken to be the average of the SAL and non-SAL estimates. I estimated the forcing over the course of a day by making hourly calculations for solar angles typical for the month of June at 15N latitude. For both the SAL and ½ SAL cases there is a net negative forcing of -9W/m^2 and -5W/m^2, respectively, throughout the day (Figure 2.10). While the net negative longwave water vapor forcing is constant throughout the day, there is a diurnal cycle to the positive shortwave water vapor forcing. During the daylight hours there is less attenuation of solar radiation by water vapor for the two SAL cases. Therefore, the range of forcing values is -2 to -6W/m^2 for the ½ SAL case, and -4 to -12W/m^2 for the SAL case (Figure 2.10).

The reduction in water vapor associated with a dust outbreak results in a negative surface forcing that is larger in magnitude than the longwave positive surface forcing associated with the dust aerosols, for optical depth values of two or less (not shown). However, the SAL and non-SAL profiles (Dunion and Marron 2008) are only for summertime cases, and therefore I cannot assume these same reductions in water vapor during the entire year. Additionally, it is likely that there is a relationship between dust optical depth and the deviation of the SAL from the non-SAL profiles, and that the SAL profiles are not spatially uniform across the basin. Therefore, it is not prudent to estimate the surface forcing of the SAL profile anomalies that are associated with dust outbreaks, until a monthly and spatially resolved relationship between dust optical depth and atmospheric temperature and humidity is determined. Therefore, this work makes only

an estimate of the surface aerosol forcing, and does not consider all of the changes in surface radiation associated with a SAL outbreak.

Up to this point the surface forcing I calculate is only valid for a clear-sky atmosphere. Next I make the assumption that during the presence of clouds either 1) no dust is present, or 2) the cloud radiative forcing dominates over that from any aerosols in the column. This assumption allows us to scale the dust forcing by the fraction of sky that is clear, for a given grid cell, or one minus the percent cloud cover divided by 100, to obtain the all-sky forcing, in a manner similar to that described in Evan et al. (2008). In this analysis I use monthly climatological values of cloudiness, calculated over the period of 1984 through 2004, from the International Satellite Cloud Climatology Project (ISCCP) (Rossow and Schiffer 1999)[7]. Total cloud cover values are available at three hour increments, allowing for excellent sampling of the diurnal cycle. Additionally, by calculating mean monthly climatological values of cloudiness, subsequent time series of dust surface forcing are not temporally biased by artifacts in the ISCCP data related to changes in satellite viewing geometry (Evan et al. 2007). Use of model-based estimates of cloudiness as an alternative to ISCCP climatological values will be further explored in Chapter 5.

Recent work has also presented evidence suggesting a positive causal relationship between mineral aerosols and stratocumulus clouds over the northern tropical Atlantic (Kaufman et al. 2005a). Fewer clouds in an mineral aerosol-free sky would serve to increase the magnitude of my estimations of dust surface forcing. However, it is difficult

---

[7] ISCCP data are available at http://isccp.giss.nasa.gov/.

to base a parameterization of this hypothesized effect on data from passive imagers alone, since cloud classification algorithms are not trained to separate dusty pixels from cloudy ones, and therefore are likely to misclassify dust-laden pixels as cloudy (Evan et al. 2006).

The four plots in Figure 2.11 demonstrate how the all-sky forcing changes when scaled by cloudiness, for a particular case study of June 1985, at roughly 15° North latitude and 27° West longitude. The leftmost plot is of the average June diurnal cycle of μ (cosine of the solar zenith angle), the next plot to the right, entitled "Clear-Sky", is my estimate of the aerosol surface forcing for the satellite based DAOD of 1.0. Here, during daylight hours, the surface forcing is dominated by the shortwave cooling. Although during hours when the sun is below the horizon the longwave surface heating by the dust is non-negligible (about $6w/m^2$), the daytime cooling is an order of magnitude stronger and of the opposite sign, peaking at roughly $-150w/m^2$. The next plot to the right shows the climatological ISCCP diurnal cycle of cloudiness at this location. The rightmost plot, entitled "All-Sky," is the diurnal cycle of the "Clear-Sky" forcing multiplied by one minus the diurnal cycle of the "Cloud Cover" divided by 100. This is our estimate of the all sky forcing. For this case the mean all sky forcing is $-30W/m^2$, which I take to be the mean monthly forcing since the DAOD value is also a monthly mean.

Figure 2.12 is a map of the mean total (IR) cloud amounts from the ISCCP record over the period of 1984–2004. Cloud cover is most persistent close to the equator, reflecting the location of the Intertropical Convergence Zone (ITCZ), and is less so further north, consistent with the descending branch of the Hadley Cell. Additionally,

cloudiness values are higher towards the center of the tropical North Atlantic basin (roughly 25-60°W), and are reduced closer to West Africa, and the American continent (not shown). This spatial pattern of cloudiness will be reflected in the maps of aerosol surface forcing that I will present later in this chapter.

2.3 Comparison of shortwave model with observations

Validation of the shortwave model is done by making comparisons against shipboard measurements of downwelling shortwave radiation at the surface in the tropical Northern Atlantic. Solar downwelling flux, as measured by a pyranometer, and aerosol optical depth, as measured by a sun photometer, from two cruises off the coast of West Africa are available for this comparison[8]. These observations were made onboard the German research vessel Polarstern during November 2007 and May 2008 (Figure 2.13)[9]. Here I compare observed flux with two-stream and STREAMER model output, based on the instantaneous observed solar zenith angle, total column water vapor, and aerosol optical thickness. Scatterplots of the observed and modelled surface downwelling solar flux show excellent agreement between both the two-stream model and STREAMER, and observations, for both cruises (Figure 2.14). It is likely that the causes of strong disagreement, most pronounced during the second cruise, result from improper cloud screening, although further testing is needed to verify this hypothesis. The bias in the comparisons with STREAMER are more pronounced than those with the two-stream model, where the STREAMER fluxes appear to be weaker in magnitude (Figure 2.14),

---

[8] Used were a Microtops sun photometer, and a Kipp & Zonen CM21 pyranometer.
[9] Data made available by Andreas Macke from IfM-GEomar in Kiel, and Stefan Kinne from the MPI for Meteorology in Hamburg.

corroborating the findings in my earlier comparisons between the two models (Figure 2.7); that STREAMER fluxes are more sensitive to aerosol forcing, suggesting that the two-stream model is more accurate in this application.

I have also plotted the two-stream model and STREAMER bias as a function of μ (Figure 2.15) and aerosol optical depth (Figure 2.16). In both of these cases there is not a clear bias dependence on either the optical depth nor the solar zenith angle. Furthermore, from these plots it is easier to see that the bias is stronger for the November cruise than it is for the May one. A plausible reason for this disconnect is that the dust from the November case is from a source region with slightly different mineral and therefore optical properties than the dust for the May case, and that the optical properties from the May dust are more similar to those assumed in our model.

2.4 Satellite climatology of surface forcing by mineral aerosols

In order to estimate the change in radiation at the surface by dust over the course of the AVHRR record I calculate the forcing at each PATMOSx ½° grid cell with my monthly mean DAOD values. This is accomplished by subtracting, at each cell, a time series of the surface radiation with DAOD set to zero, from a time series of the surface radiation with DAOD values reflected by my satellite estimates. Averaged over the northern tropical Atlantic dust forcing has an annual cycle (Figure 2.17) around the mean forcing of -4W/m^2 that reflects the seasonality of West African dust outbreaks, with peaks in activity during the boreal winter and summer (Figure 2.3), and a minimum in the magnitude of forcing in November. That mineral aerosol forcing so closely follows the DAOD is not surprising since the forcing is instantaneous. The 27 year time series of

monthly forcing values also averaged over the northern tropical Atlantic (Figure 2.17) shows that the annual peak in the magnitude of dust forcing has gone from the maximum in 1985 of nearly -10W/m^2, to the minimum of -6W/m^2 in 2005. Additionally, annually averaged dust forcing has declined by about 2W/m^2 over the course of the AVHRR record, with the strongest and weakest forcing also observed during 1985 and 2005, respectively.

Using the monthly values of SAOD, I also calculate a time series of stratospheric aerosol forcing. Although the relationship between dust and H$_2$SO$_4$ forcing is nearly linear (Figure 2.6), here I subtract a series of the surface radiation with SAOD set to zero and DAOD equal to the annual cycle, from a series of surface radiation forced only by the DAOD annual cycle. SAOD surface forcing is non-zero only for H$_2$SO$_4$ plumes that are associated with the volcanic eruptions of El Chichón in 1982 and Mt Pinatubo in 1991 (Figure 2.18). With each volcanic event, the surface forcing decays to zero roughly three years after the eruption. I calculate that averaged over the north tropical Atlantic, SAOD associated with El Chichón and Mt. Pinatubo result in surface forcing maximums (in magnitude) of -7W/m^2 and -5W/m^2, respectively. Furthermore, the magnitude of the SAOD forcing (Figure 2.18) during the peak of each volcanic event is similar in magnitude to the mean of DAOD forcing over the course of the satellite record (Figure 2.17).

To estimate the combined surface forcing from mineral and stratospheric aerosols, I subtract calculated surface radiation for an aerosol-free sky from calculated surface radiation that reflects my values of DAOD and SAOD, at each grid cell. This time series

of the combined DAOD and SAOD forcing (Figure 2.19) is almost a superposition of the individual forcing series (Figure 2.17 and Figure 2.18). The monthly time series of aerosol forcing shows the strong annual cycle of the dust forcing, and the smoothed time series shows the relative maximums in the magnitude of surface forcing occurring at the beginning of the record in 1983, and then in 1992 (Figure 2.19). However, since the DAOD forcing was the strongest from the period of 1982–1986 (Figure 2.17), this peak in forcing for the mineral and stratospheric aerosol case (Figure 2.19) does not fall off as strongly as does the stratospheric only one (Figure 2.18). This smoothed series shows a range of $5W/m^2$, with the strongest and Weakest forcing for occurring in 1983 ($-9W/m^2$) and 2005 ($-4W/m^2$), respectively. Additionally, the time series of annual forcing maximums (in magnitude) has a peak of nearly $-15W/m^2$ in 1982, and a minimum of $-6W/m^2$ in 2005, almost equivalent to the series mean value of $-5W/m^2$, and reflects a forcing range of $9W/m^2$.

The spatial distribution of the climatological forcing (Figure 2.20), a mean over all available months, is very similar to that of the DAOD (Figure 2.1), reflecting strongly the position of the summertime maximums in dust loading, but is also modulated by cloud cover variability (Figure 2.12). The strongest forcing values are found close to West Africa, and between the latitudes of 10 and 20°N. These large values, which are less than $-10W/m^2$, become weaker to the west, roughly falling off at a rate of about $-2.5W/m^2$ per degree longitude. Forcing is almost zero within about 5° latitude of the equator, and near the northernmost extent of my domain at 30°N.

Since I use climatological monthly values of cloudiness for this study, it is possible that I do not capture variability in surface forcing that is only associated with changes in cloudiness. Observations of cloud cover from PATMOSx are twice daily from the period of 1982 through 1995, and four times daily afterwards. While I have yet to uncover temporal artifacts in PATMOSx, a sampling of twice daily is not sufficient to describe the diurnal cycle of clouds. Therefore, to determine if year-to-year changes in cloudiness play a non-negligible role is determining changes in aerosol forcing I also ran my forcing analysis using NCEP Reanalysis (Kalnay et al. 1996) total cloud cover, which has a four times daily sampling. My resultant time series of the aerosol forcing was little changed using the reanalysis data, which may not be entirely surprising since aerosols are often found in regions with low (in percentage) cloud cover. Therefore, in the remainder of this work I opt to use cloud diurnal cycles that are calculated from ISCCP data since the diurnal sampling is better than that from the model data.

2.5 Figures
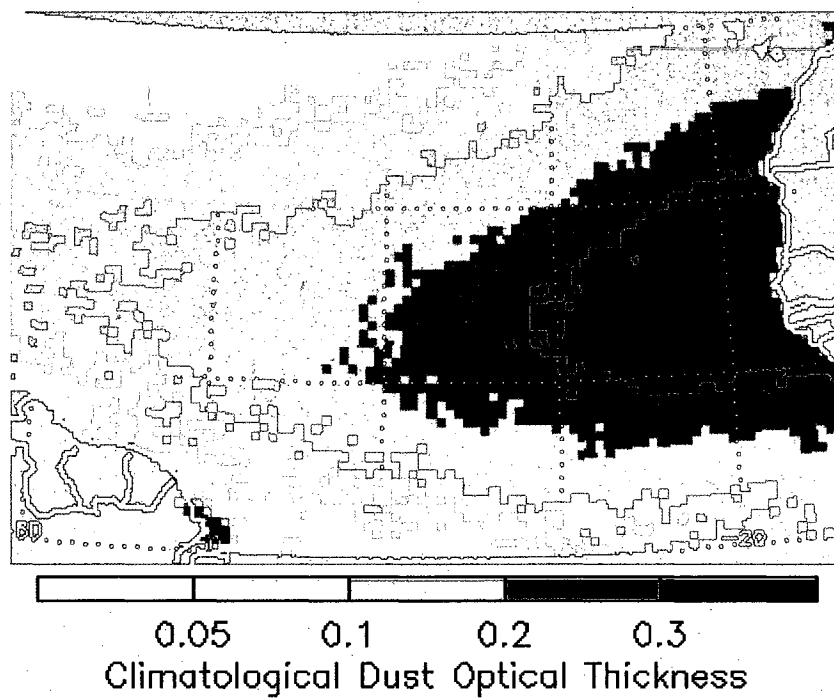
Figure 2.1. Climatological map of Dust Aerosol Optical Depth (DAOD). Here, DAOD values are based on AVHRR AOT retrievals for the period of 1982–2007, and are only present over water.
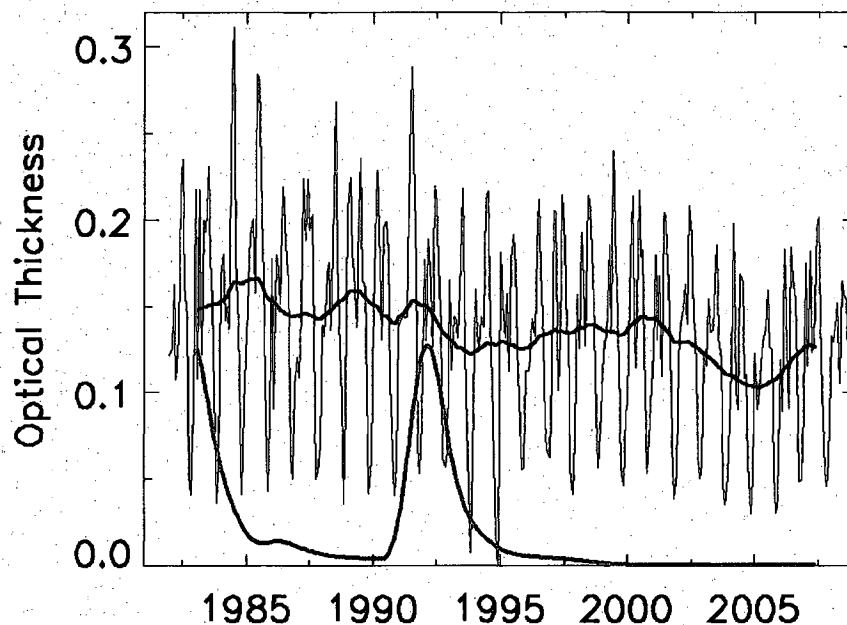
Figure 2.2. Monthly time series of DAOD and SAOD averaged over the tropical North Atlantic (0-30N & 15-65W). The thin black line is the monthly time series of DAOD, and the thick black line is a smoothed version of the monthly data. The thick grey line, with peaks starting in 1982 and 1991, is a smoothed monthly time series of SAOD.
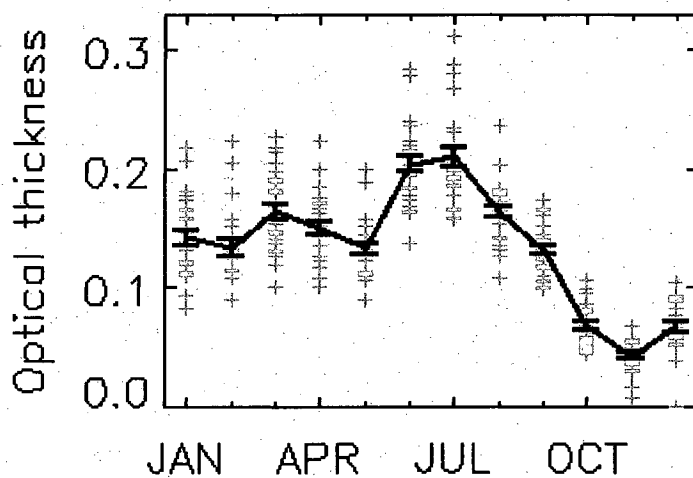
Figure 2.3. Seasonal cycle of DAOD. The black line is the monthly seasonal cycle of DAOD averaged over the tropical North Atlantic (0-30N & 15-65W) for the period of 1982–2007. The error bars represent the standard error on the estimation of the mean monthly values. The grey crosses are plots of the individual monthly mean values for all years in the analysis.
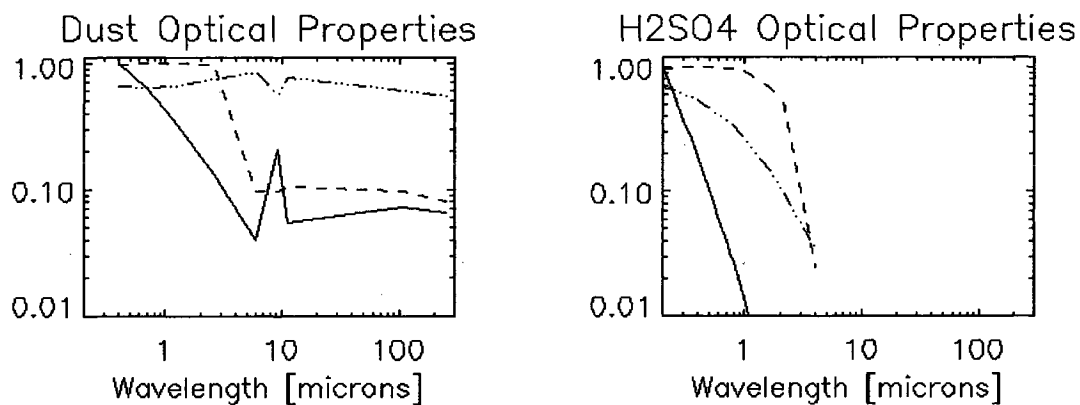
Figure 2.4. Optical properties of mineral and stratospheric aerosols. Both plots show the aerosol single scatter albedo (dashed line), asymmetry parameter (dash-dotted line), and extinction coefficient (solid line, scaled to unity at 650nm) for dust (left) and H_2SO_4 (right). These optical properties are used in my radiative transfer modeling efforts to estimate the aerosol surface forcing. All values are plotted on a log x and y axis.
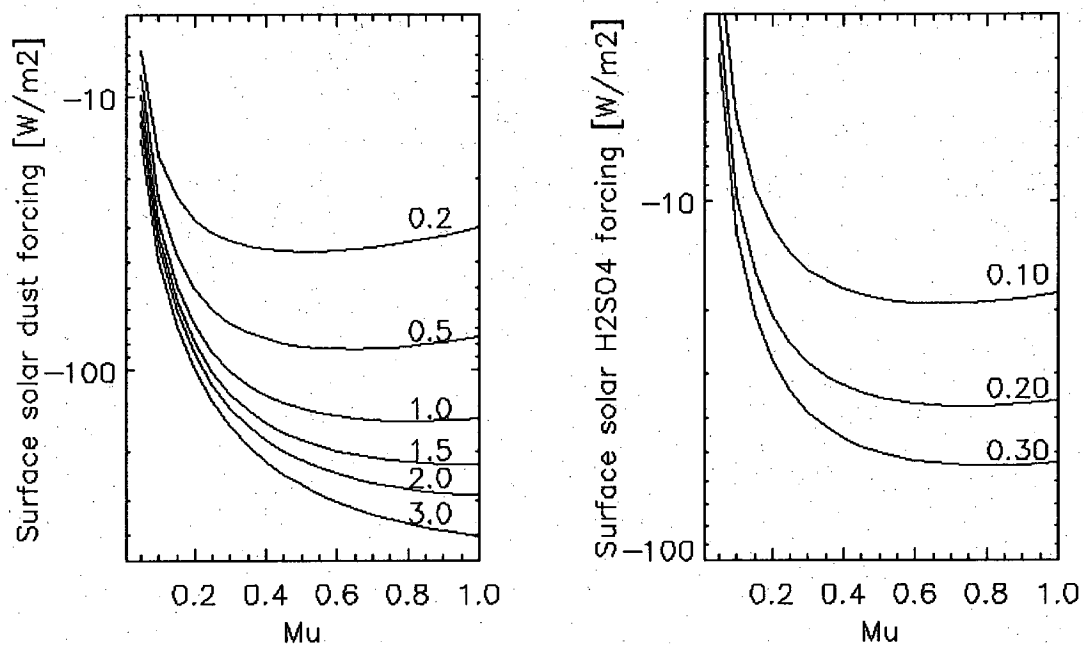
Figure 2.5. Calculations of the surface solar forcing. Figure 5a shows the surface solar forcing for various values of dust optical thickness as a function of mu. Optical thickness values are noted on the right-hand side of the line denoting their respective forcing values. The description for Figure 5b is the same except for the stratospheric aerosol case.
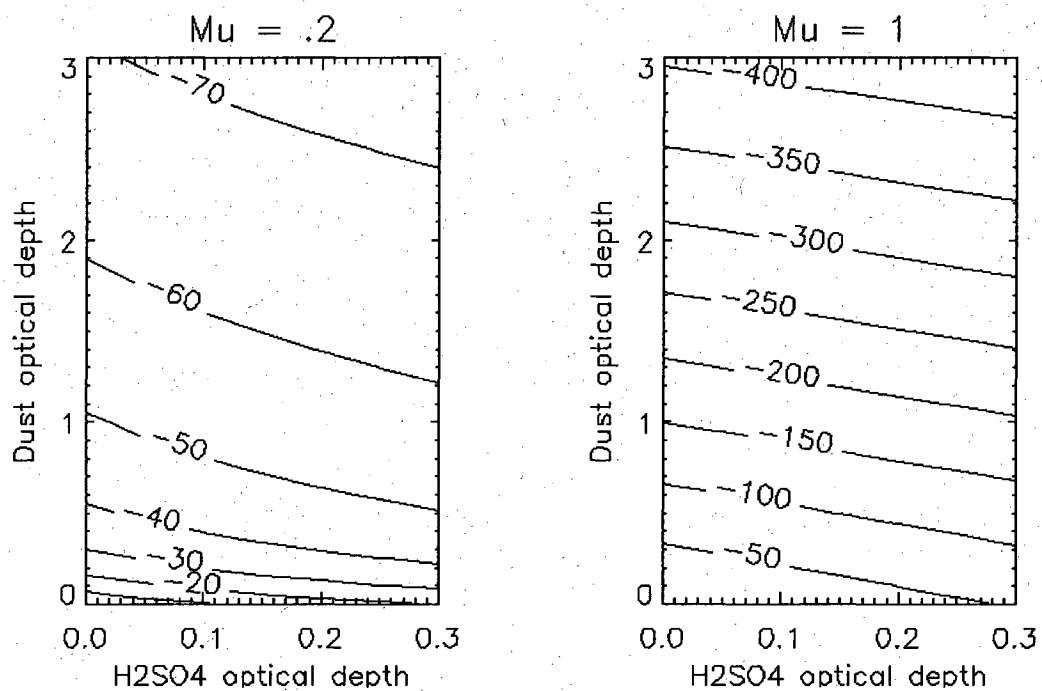
Figure 2.6. Surface solar forcing for both dust and stratospheric aerosols. All forcing calculations for panel A are for mu equals 0.2, and forcing calculations in panel B are for mu equal to one.
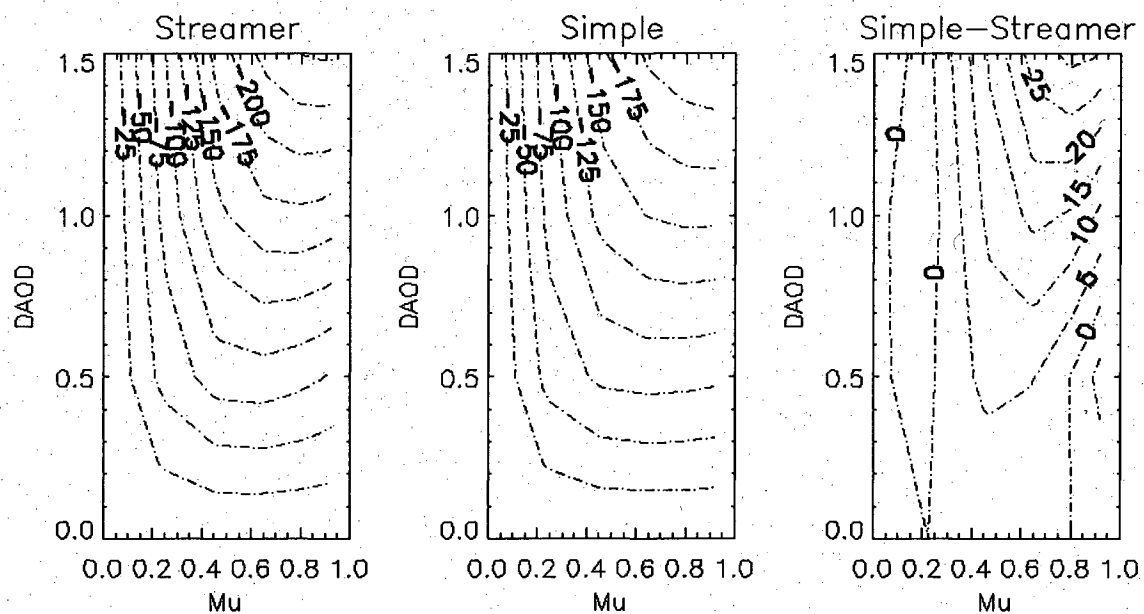
Figure 2.7 Comparison of shortwave surface forcing from Streamer and the simple model described here. Shown are Streamer estimates (left panel), those from our simple model (center panel), and the difference, or forcing from our simple model minus those from Streamer (right panel). Forcing is shown as a function of μ and DAOD, with SAOD equal to zero.
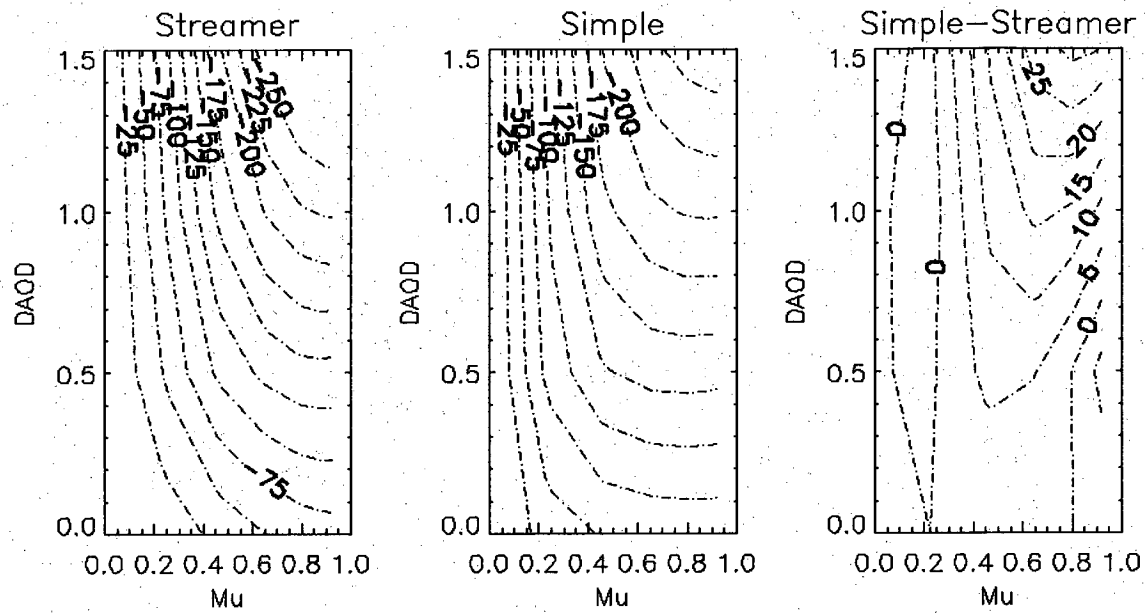
Figure 2.8 Description is the same as for Figure 2.7, except that here forcing values are for SAOD = 0.2.
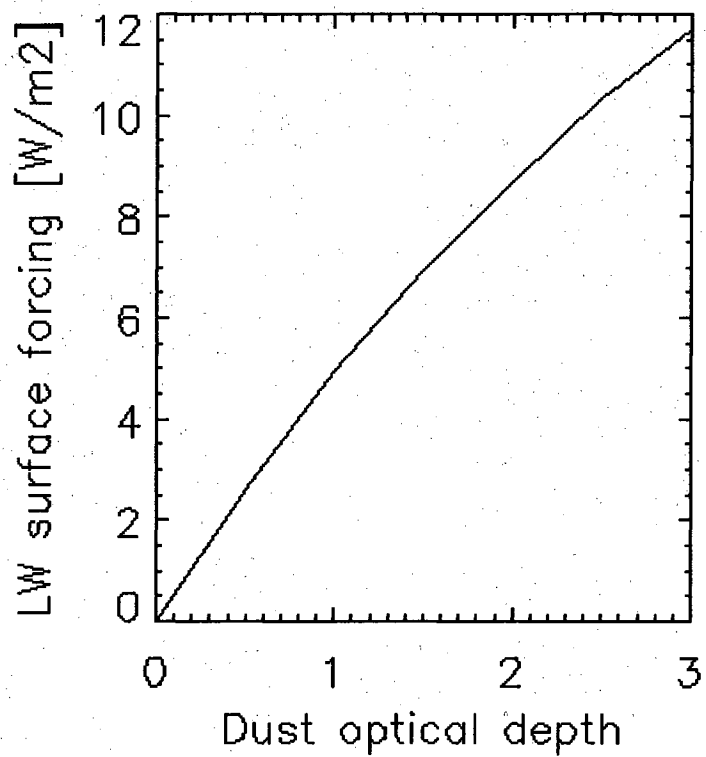
Figure 2.9. Surface longwave forcing by mineral aerosols. Forcing calculations as a function of dust optical depth made using the STREAMER radiative transfer model.
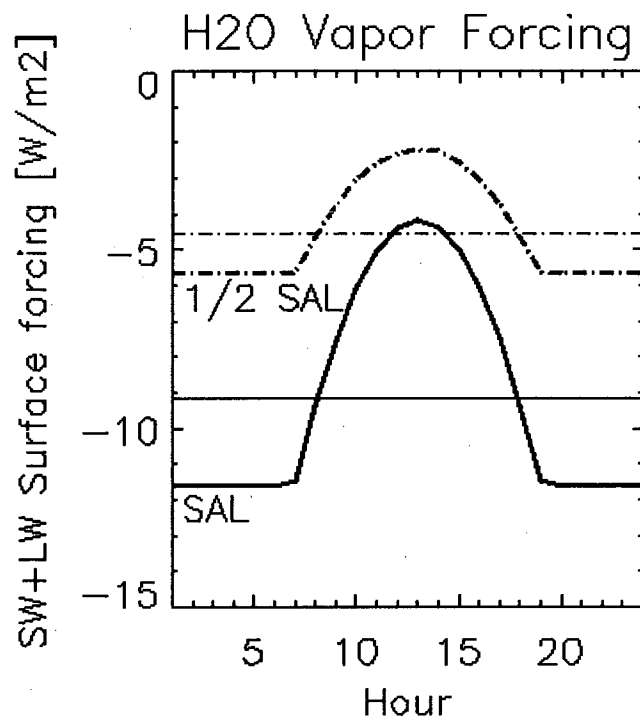
Figure 2.10. Surface longwave and shortwave water vapor forcing by the SAL.
Forcing calculations as a function of dust optical depth made using the STREAMER
radiative transfer model.
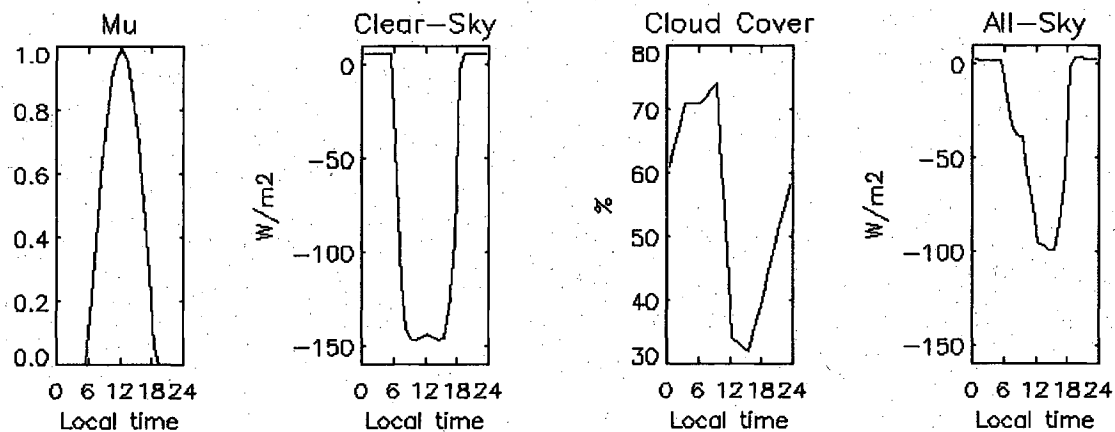
Figure 2.11. Diurnal plots of mu, clear-sky dust surface forcing, cloud cover, and the all-sky dust surface forcing for June 1985 at 15° N & 27° W (DAOD of 1.0). The plot furthest to the left is the diurnal cycle of mu, the center-left plot is the clear-sky dust surface forcing, the center-right plot is cloud cover, and the rightmost plot is the all-sky dust surface forcing.

Climatological Cloud Cover [%]
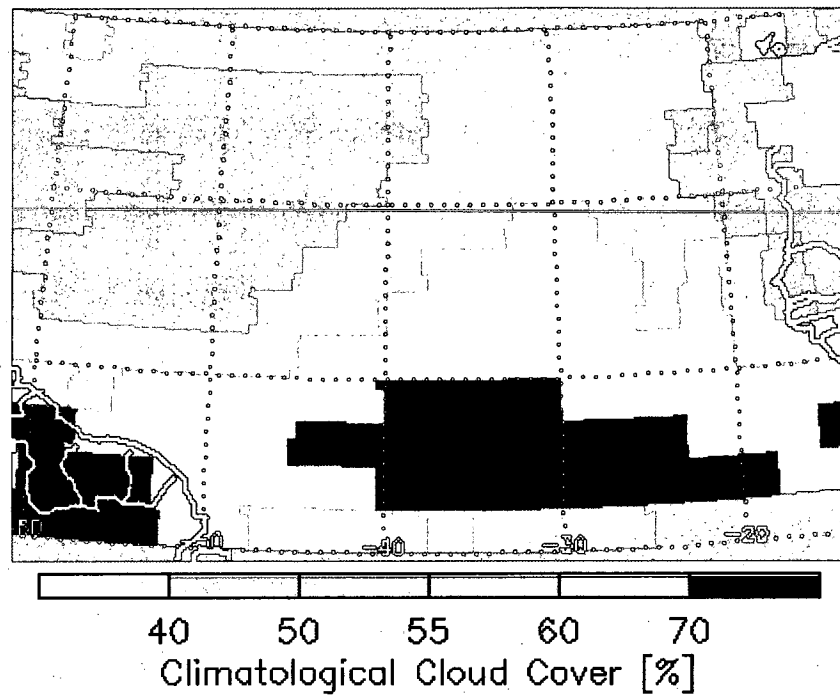
Figure 2.12. Mean total cloudiness for the period of 1984–2004. Data are IR total cloud amounts from ISCCP.
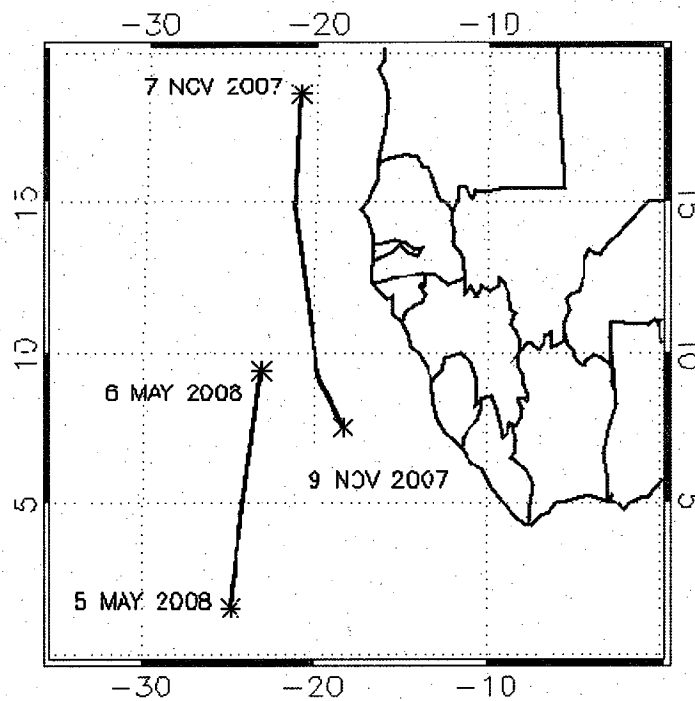
Figure 2.13 Map of ship tracks and times for the days when comparisons between my model and observations are made. Track number one starts on November 7th 2007, and track number 2 starts on May 6th 2008.
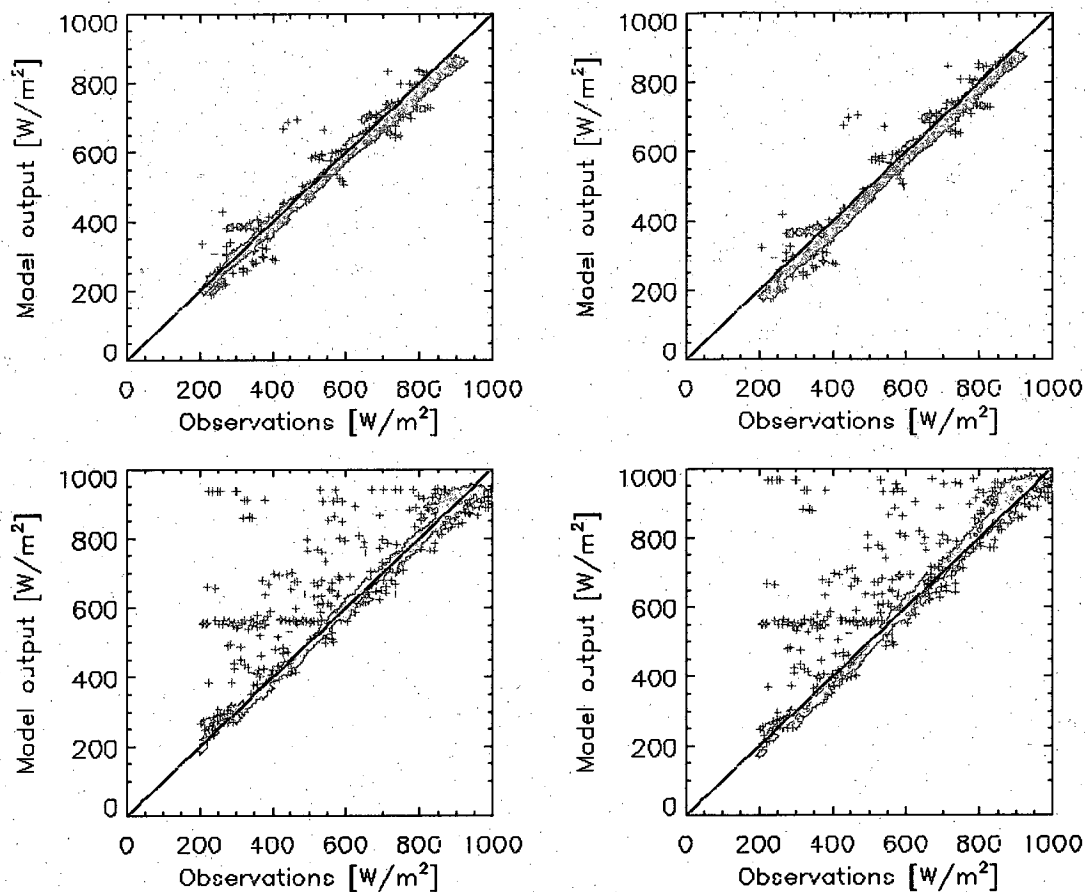
Figure 2.14 Scatterplots of comparisons between modeled and observed surface solar downwelling flux. The top plots are made using data from the first ship track (November 2007), and the bottom plots are made using data from the second one (May 2008). The modeled flux from the plots on the left is output from my simple two-stream model, and the modeled flux on the right is output from STREAMER.
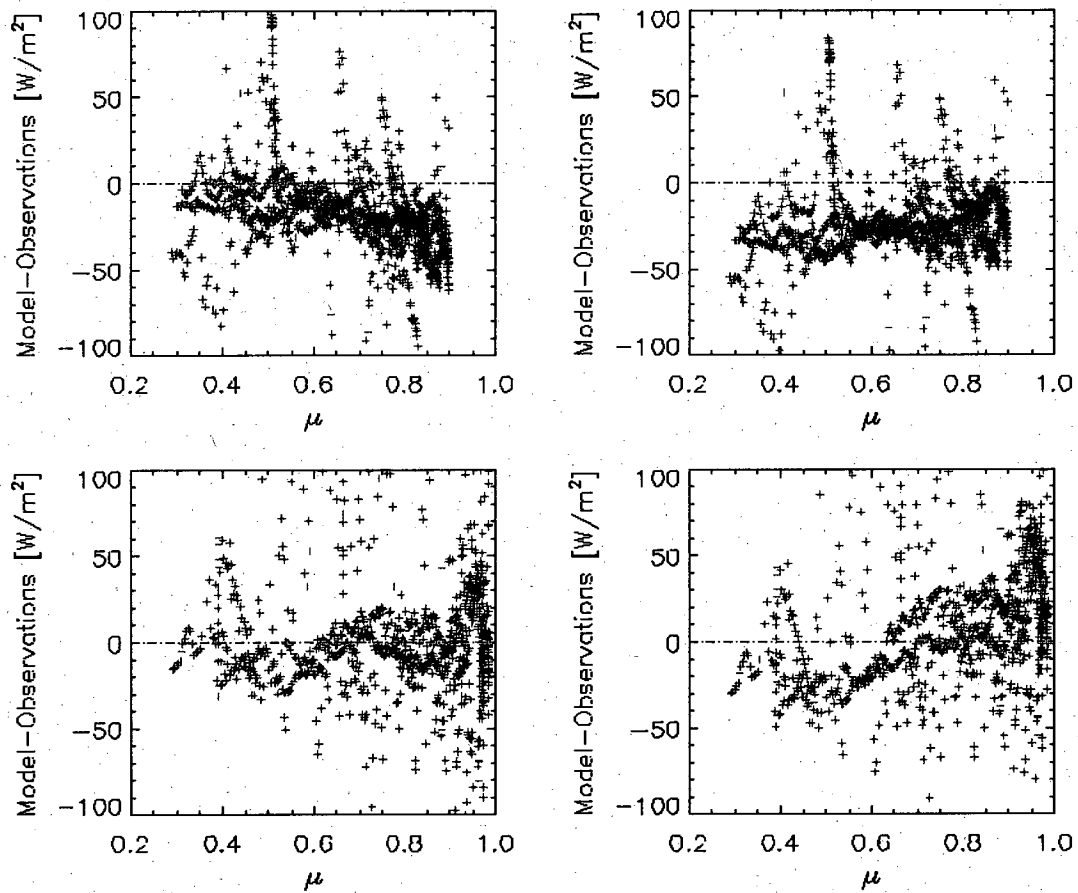
Figure 2.15 Scatterplots of the bias between modeled and observed surface downwelling solar flux, as a function of the cosine of the solar zenith angle. Otherwise, description is the same as for Figure 2.14.
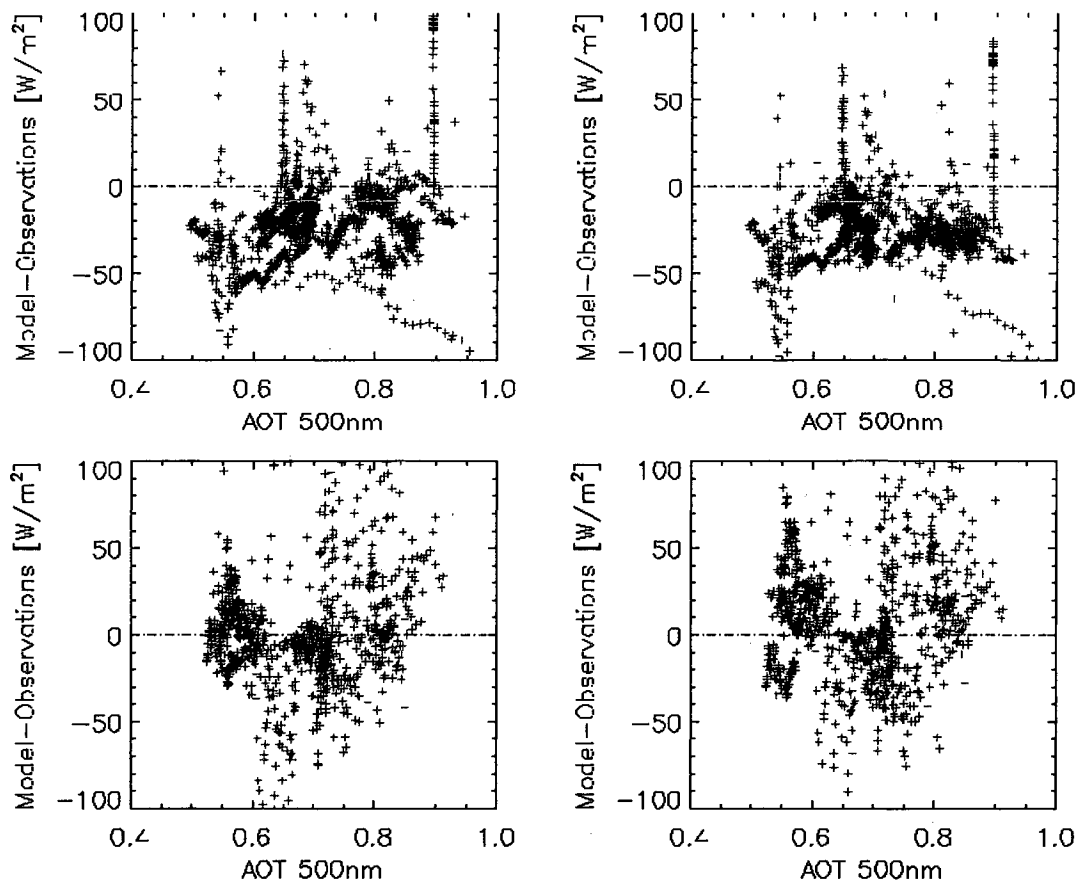
Figure 2.16 Scatterplots of the bias between modeled and observed surface downwelling solar flux, as a function of observed aerosol optical thickness at 500nm. Otherwise, description is the same as for Figure 2.14.
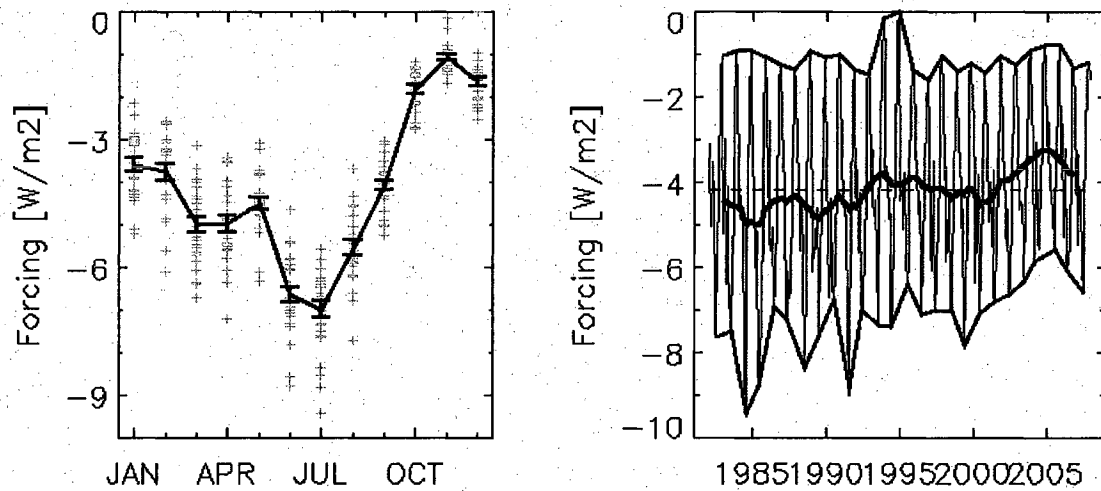
Figure 2.17. Annual cycle and time series of dust surface forcing averaged over (0-30N & 15-65W). The plot on the left is the annual cycle of dust forcing, where error bars represent uncertainty in the estimate of the mean values. On the right, the thin line is the monthly forcing values, the thick black lines bounding the upper and loÏr values represents annual minimums and maximums, respectively, and the thick time series running though the monthly values is the month time series smoothed with two recursive 13-month running mean filters.
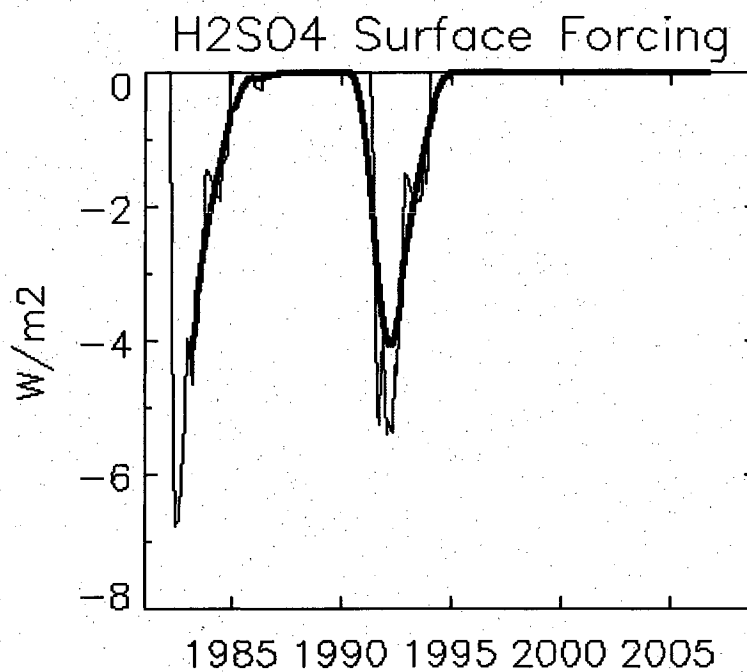
Figure 2.18. Time series of mean SAOD surface forcing over the north tropical Atlantic (0-30N & 15-65W). The thin line is a monthly time series of calculated surface forcing, and the thick line is the monthly series smoothed with two recursive 13-month running mean filters.

Dust+H2SO4 Surface Forcing
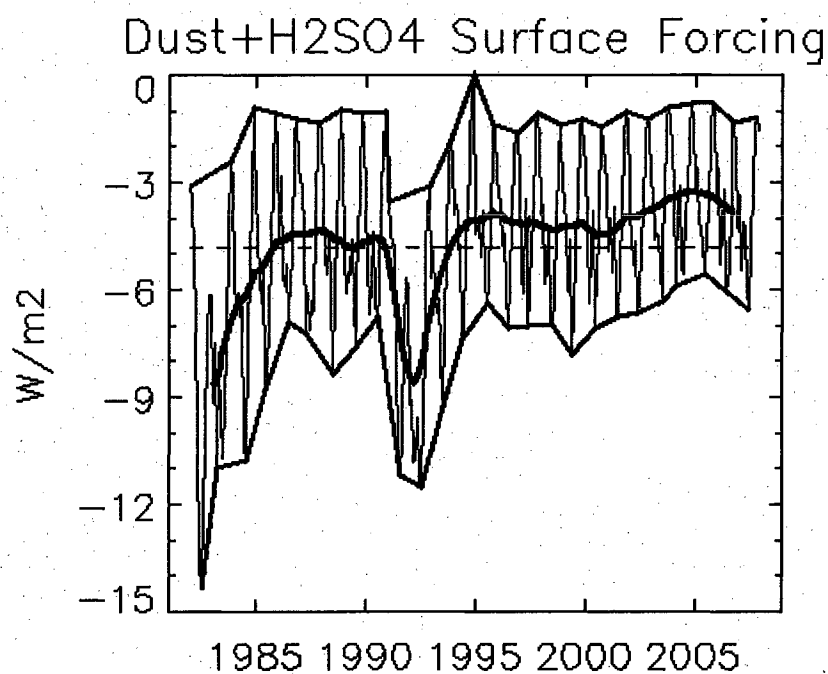
Figure 2.19. Time series of DAOD and SAOD surface forcing averaged over the north tropical Atlantic (0-30N & 15-65W). The thin line is the monthly forcing values, the thick black lines bounding the upper and loIr values represents annual minimums and maximums, respectively, and the thick time series running though the monthly values is the mean annual time series smoothed with two recursive 13-month running mean filters.
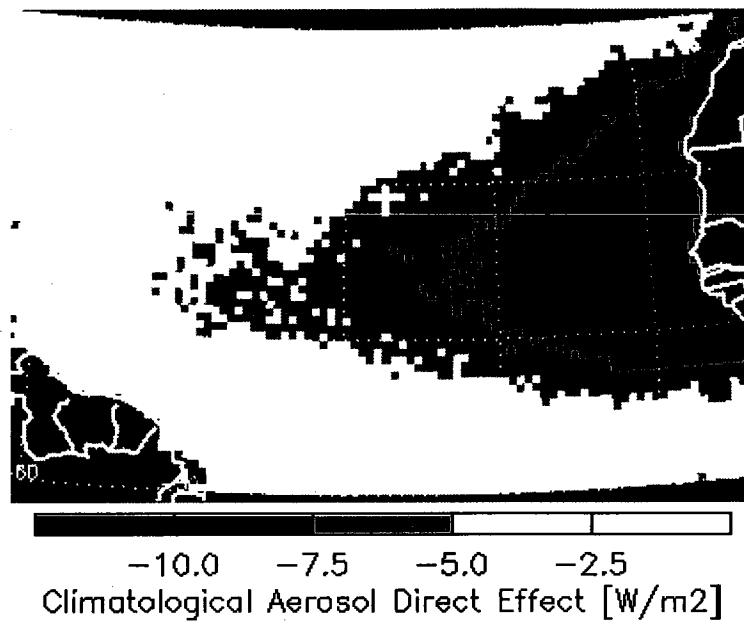
Figure 2.20. Climatological map of mineral and stratospheric surface aerosol forcing. Forcing means are based on monthly values from the period 1982–2007.

3 Modeling the response to aerosol surface forcing

3.1 The simple stochastic model

Evan et al., (Evan et al. 2008) used satellite-based estimates of aerosol surface forcing to calculate the instantaneous change in temperature of the ocean mixed-layer. Here, in addition to improving the forcing climatology, I also go one step further by attempting to model the integrated oceanic response to forcing by aerosols over the north tropical Atlantic. One simple way to estimate this response is to use a stochastic ocean temperature model with a variable mixed-layer depth (Deser et al. 2003). This model is an extension of the simple stochastic climate model (Frankignoul and Hasselmann 1977), in that it includes a mechanism for reemergence of sea surface temperature (SST) anomalies.

From Deser et al. (2003), the governing equation for the simple stochastic model (Frankignoul and Hasselmann 1977) is

$$\frac{\left(\rho C_p H_{eff}\right)dT'}{dt} = F - \lambda T', \tag{3.1}$$

where ρ is the density of sea water, Cp is the specific heat of sea water, H_{eff} is the mean annual mixed layer depth, T' is the temperature anomaly of the mixed layer, t is time (in units of months for this analysis), F is an atmospheric forcing of T', and $\lambda T'$ is the linear damping coefficient. The damping term $\lambda T'$ is a idealized parameterization of the turbulent latent and sensible heat fluxes from the ocean to the atmosphere that are associated with T'.

Several methods exist for deriving λ, including linearizing the bulk formulas for the sensible and latent heat fluxes associated with T' (Barsugli 1995), or calculating from the output of a general circulation model (Deser et al. 2003). Assuming that the decorrelation timescale for atmospheric variability is much short than changes in SST, F

in Equation 1 can be assumed to be a white noise process, then λ can be estimated using the autocorrelation function of T',

$$r(\tau) = \exp\left\{-\frac{\lambda}{\left(\rho C_p H_{eff}\right)}\tau\right\},$$

(3.2)

so that

$$\lambda = \ln(r(\tau))\left(-\frac{\left(\rho C_p H_{eff}\right)}{\tau}\right).$$

(3.3)

I use climatological values of monthly autocorrelation in SST from observations and a climatology of mixed layer depths (de Boyer Montégut et al. 2004) (Figure 3.1) to calculate spatially explicit values of λ (Figure 3.2). I also solved for $\lambda(t)$, with t being a function of month, and using monthly climatological values of H, and r, but this did not substantially alter my final results, so here I use a value of λ that is spatially explicit but constant in time for simplicity.

3.2 Reemergence and the stochastic model

Reemergance, as it applies to SST anomalies, describes the physical process by which wintertime SST anomalies are entrained below the mixed layer, during the transition to summer when the mixed layer shoals, then reemerge when the mixed layer deepens again, during the transition back to the winter. To demonstrate this reemergence mechanism in observations, it is useful to first look at a plot of the seasonal cycle of the mixed layer depth over the tropical north Atlantic (Figure 3.4). Here, from depth estimates described in de Boyer Montegut et al. (2004)[10], and averaged over the region of 0–30°N & 15–65°W, the layer is deepest in January and February (about 47m) and most shallow during July and August (roughly 24m). As the mixed layer deepens during

---

[10] Climatological mixed layer depths downloaded from the website of de Boyer Montegut, http://www.locean-ipsl.upmc.fr/~cdblod/mld.html.

the fall months it entrains water from below the layer, and as the mixed layer shoals in the spring months it is reforming at a more shallow depth. It is worth noting that, from Equation 3.1, SST is most sensitive to changes in atmospheric forcing from June through September, and that mineral aerosol forcing is strongest during the months of June and July (Figure 2.3). This temporal collocation of enhanced SST sensitivity and heavy surface forcing conspire to make the tropical north Atlantic particularly strongly influenced by summertime dust outbreaks from West Africa.

Having in mind the seasonality of the mixed layer (Figure 3.4), I expect that SST anomalies present from February through May will be trapped and effectively insulated below the mixed layer as it shoals and reforms at more shallow depths. These subsurface anomalies will be re-entrained into the mixed layer (reemerge) as the mixed layer deepens and mixes up the deeper water, from October through January. To demonstrate this I show a plot of SST autocorrelation based on a monthly detrended time series of SST from the Hadley Centre (Rayner et al. 2003), averaged over 0–30°N & 15–65°W and for the time period of 1955–2004 (Figure 3.5). Here, the region of strong positive correlation coefficients that extends diagonally downward and in the direction of increasing lag (to the right) represents this reemergence mechanism. For example, March SST is well correlated with SST during the months of November, December, and January. Referring back to the mixed layer depth annual cycle (Figure 3.4), the layer shoals from roughly 42 to 35m from March to April. Therefore, the March SST anomalies are insulated below the summer mixed layer, and then are remixed into the layer (and impact observed SST) when the depths again deepen through 42 to 35m, which occurs during the months of November through January.

The pattern of strong positive correlation coefficients seen in Figure 3.5 that start at September with a lag of two months and then extend downward and to the right, can be

attributed to the reemergence mechanism. Therefore, to capture the SST response to aerosol forcing over the tropical north Atlantic, it is imperative that the stochastic model is able to reproduce this effect. It is also worth noting the area of high correlations centered on October SST anomalies and extending all the way to a lag of 23 months (i.e., October SST anomalies are correlated with October SST anomalies some two years later). It is not clear why October (and to a lesser degree September) SST anomalies in detrended data are so persistent, and investigation into this effect is beyond the scope of this thesis.

Deser et al. (2003) incorporated reemergence into the simple stochastic model (Eqn. 3.1) by introducing a variable mixed layer $H(t)$, and an entrainment velocity $W_e = dH(t)/dt$, giving

$$\frac{(\rho C_p)d(H(t)T)'}{dt} = F' - \lambda T' + (\rho C_p W_e)(T' - T_b').$$ (3.4)

Here, T_b' is the temperature anomaly below the mixed layer, which formed at an earlier time, which I model to dissipate with an e-folding time scale of three years. In my case, $H(t)$ is a monthly climatology of the mixed layer depth (de Boyer Montégut et al. 2004), and λ is from Equation 3.2. When the mixed layer is deepening the right-most term in Equation 3.4 act to change the anomalous heat content by entrainment, and when the mixed layer is shoaling the term is zero.

Using a 50-year monthly white noise time series for F' I integrate Equation 3.4 forward in time at each of my model grid cells in order to test the validity of the stochastic model over the domain of 0–30°N & 15–65°W. I next calculate the autocorrelation of the output (Figure 3.5) in order to make a direct comparison with observations (Figure 3.6). The structure and magnitude of the autocorrelation of the mixed layer temperatures from the model output (Figure 3.6), compares very well to

observations (Figure 3.5) with respect to both the structure and magnitude of the correlation coefficients. Reemergence, as demonstrated by the region of high correlations extending downward and to the right that start in the boreal fall months (with zero-lag), is clearly reproduced in the stochastic model, and mirrors that from observations. The model also reproduces the two to three month persistence in temperature anomalies that are observed throughout the year.

3.3 Forcing the stochastic model with estimates of the aerosol direct effect

As I have estimated the surface forcing by mineral dust and stratospheric aerosols it is possible to estimate 1) the climatological mixed layer temperature response dust ($T_{d_{seasonal}}$), 2) the monthly mixed layer temperature response to dust for the period of 1982–2007 (T_d), 3) the monthly mixed layer temperature response to stratospheric volcanic aerosols for the period of 1982–2007 (T_s), and 4) the monthly mixed layer temperature response to combined dust and stratospheric volcanic aerosols for the period of 1982–2007 (T_{d+s}). To estimate these four mixed layer responses I need to complete three separate runs of the stochastic model, each time defining F' from Equation 3.4 as

$$F' = F_{d_{seasonal}}$$
$$F' = F_d \qquad\qquad (3.5)$$
$$F' = F_{d+s}$$

where $F_{d_{seasonal}}$ is the seasonal cycle of dust surface forcing, F_d is the 30-year monthly time series of dust forcing, and F_{d+s} is the 26-year monthly time series of the dust and stratospheric aerosol surface forcing. Therefore, $T_{d_{seasonal}}$ is the output from the $F' = F_{d_{seasonal}}$ run, T_d is obtained by initializing the model with the last year of the $T_{d_{seasonal}}$ run then integrating forward with $F' = F_d$, T_{d+s} is obtained by initializing with the last year of the $T_{d_{seasonal}}$ run then integrating forward with $F' = F_{d+s}$, and $T_s = T_{d+s} - T_d$.

More specifically, we define $T_{d_{seasonal}}$ as the last 12 months of mixed layer temperatures after a 30-year run with $F' = F_{d_{seasonal}}$, although equilibrium (loosely defined as a mean annual mixed layer temperature response to the season dust forcing that is constant from one year to the next, out to three significant digits) is reached after six years (Figure 3.7). The annual cycle of dust cooling, defined as the last year from the spin up model run, has a maximum in the magnitude of dust cooling during the months of July, August, and September (Figure 3.8), lagging the maximum in dust cover by two to three months, but in phase with the seasonal cycle of the mixed layer (Figure 3.4).

The spatial pattern of the climatological cooling by dust (Figure 3.9) is strongly indicative of the distribution of dust optical depth (Figure 2.1), cloud cover (Figure 2.12), and lambda (Figure 3.3). Based on the mean annual mixed layer response to the dust surface forcing, mineral aerosols exert their strongest influence on ocean temperatures, about -1.0 to -2.0°C, between the latitudes of 10°-20°N and, east of 30°W or between the latitudes of 45-55°W. There is little to no dust forcing of mixed layer temperatures west of -20°W and either north of 25°N or near the equator (Figure 3.9). Broadly speaking, the magnitude and spatial extent of temperature response is similar to that from estimations made from the output of an atmospheric general circulation model coupled to a slab ocean model (Yoshioka et al. 2007), and the mean annual response of the mixed layer temperature to the dust seasonal cycle is -0.60°C.

In order to estimate T_d I initialize the stochastic model with the model state from the final year of the 30-year $F' = F_{d_{seasonal}}$ run, and then force the model with the 26-year monthly time series of dust surface forcing (Figure 2.17), or $F' = F_d$. From the model output T_d has a strong seasonal cycle (Figure 3.8) that is superimposed over more coherent interannual variability (Figure 3.10). The monthly maximum in the magnitude of dust cooling occurs in August of 1985, and the minimum in magnitude in April of

2005. Stronger cooling by dust is observed primarily prior to 1992, and weaker than average cooling occurs primarily after 2000 (thick black line, Figure 3.10), and the annual mean maximum and minimum in magnitude of T_d occur in 1985 and 2005, respectively. This temporal pattern of stronger cooling towards the beginning of the record suggests an overall weakening in the mineral aerosol direct effect over the northern tropical for the last 26 years. This apparent trend will be explored further in Chapter 4.

I next force the stochastic model, initialized by the last year from the model spin up run, with $F' = F_{d+s}$ in order to estimate T_{d+s}. The main distinction between the time series of T_d (Figure 3.10) and T_{d+s} (Figure 3.11) is the inclusion of the surface forcing associated with the eruptions of El Chichón in 1982 and Mt. Pinatubo in 1991, The maximum in the magnitude of the monthly temperature forcing for each of these events by both mineral and stratospheric aerosols is -1.30°C in September 1982 (Chichón) and -1.24°C in August 1992 (Pinatubo). Annual mean maximums in the magnitude of the mixed layer temperature response are -1.11°C in 1983 and 1992 for the Chichón and Pinatubo events, respectively. While the structure of T_{d+s} differs strongly from T_d, the transitory forcing from the volcanic events only increases the mean magnitude of the response by 0.09°C (Figure 3.11). Additionally, the spatial pattern and magnitude of temporally averaged T_{d+s} (Figure 3.12) is nearly identical to that from $T_{d_{seasonal}}$ (Figure 3.9).

I lastly consider the response to only the stratospheric aerosol forcing, $T_s = T_{d+s} - T_d$. Averaged across the northern tropical Atlantic, the volcanic induced anomalies in T_s decay to zero roughly within six years (Figure 3.13). There is a slight seasonal cycle in T_s, which is driven by the annual cycle of incoming solar radiation and mixed layer depth, and averaged over the period of 1982–2007 T_s is 0.09°C. The

maximum in the magnitude of T_s associated with the eruption of El Chichón is about -0.7°C, and -0.6°C from the eruption of Pinatubo (Figure 3.13). The spatial structure of time averaged T_s (Figure 3.14) is distinct from T_{d+s} (Figure 3.12) and $T_{d_{seasonal}}$ (Figure 3.9). T_s is much more uniform across the northern tropical Atlantic basin, and is strongest closer to the coast of South America, and north of about 22°N is less than 0.05°C. The pattern of T_s (Figure 3.14) closely reflects the spatial distribution the map of monthly SST autocorrelation (Figure 3.2), which is proportional to the feedback parameter λ (Figure 3.3).

3.4 Figures
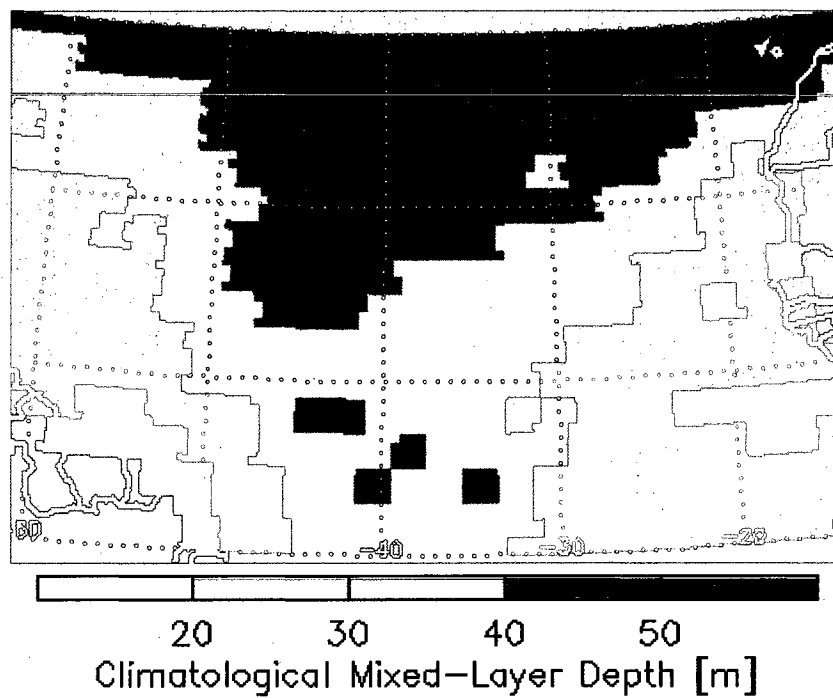
Figure 3.1 Climatological maps of the ocean mixed layer depth. Depths are from (de Boyer Montégut et al. 2004).

Climatological SST Autocorrelation
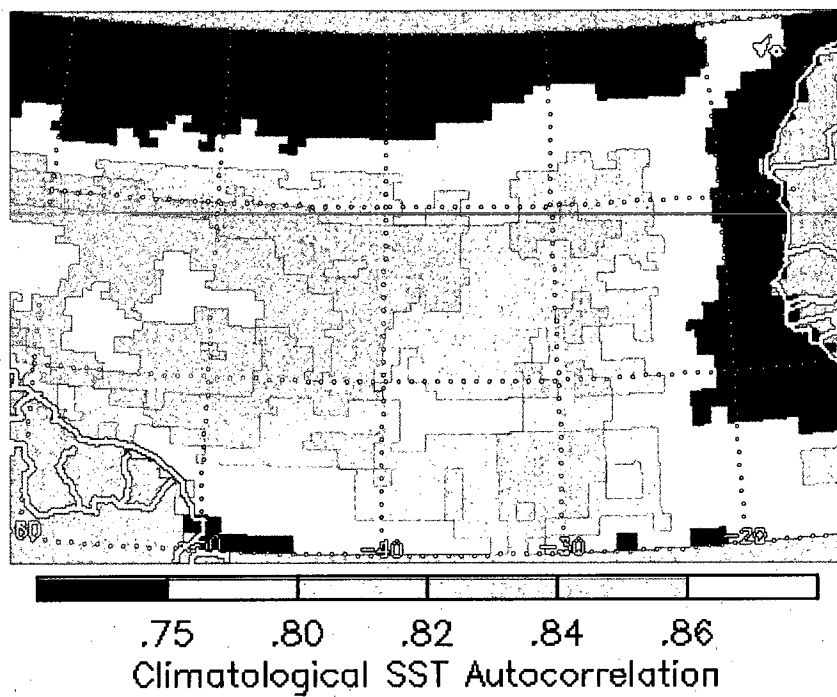
Figure 3.2 1-lag monthly SST autocorrelation based on data from 1950–2005. Autocorrelations are calculated using the HADLEY HISST data.
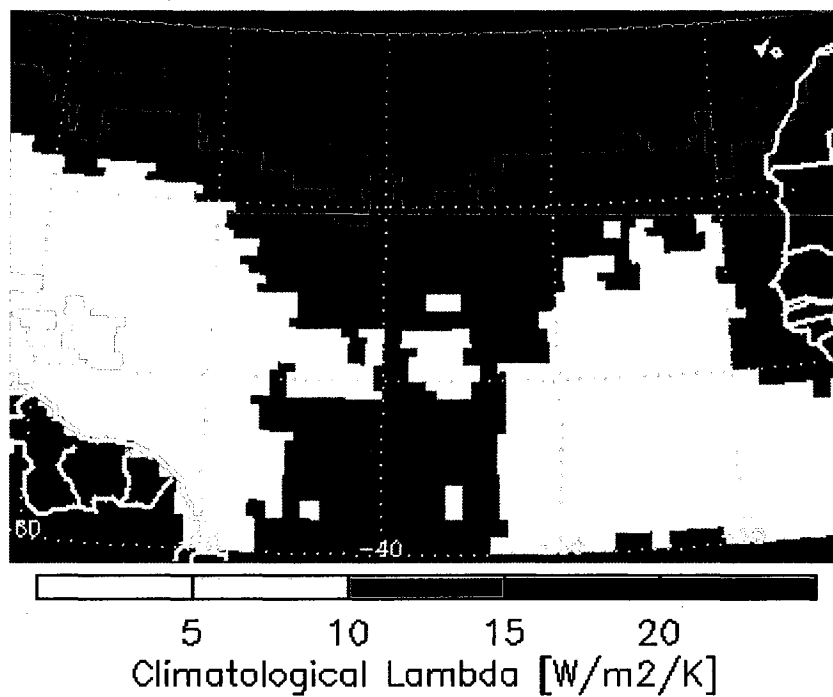
Figure 3.3 Climatological map of λ. Here, λ (Eqn 3.2) is spatially dependant on climatological mixed layer depth (Figure 3.1) and 1-lag monthly SST autocorrelation (Figure 3.2).
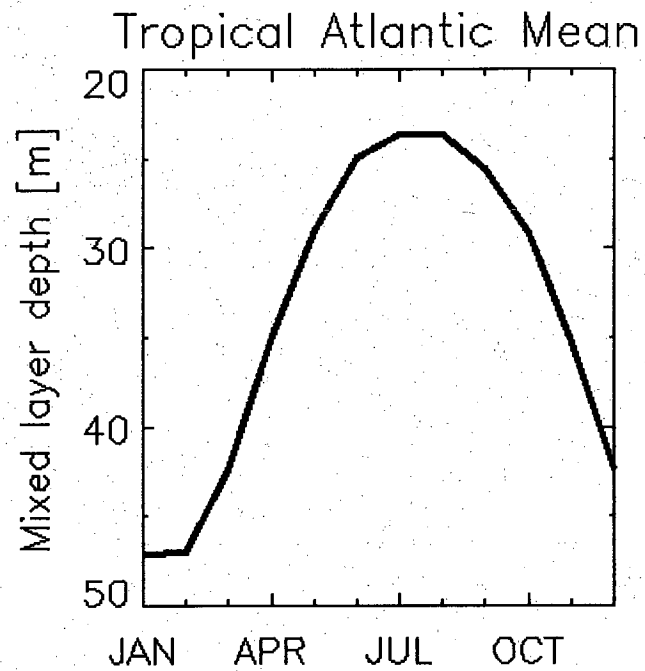
Figure 3.4 Northern tropical Atlantic mixed layer depth seasonal cycle, The plot on the left is of the seasonal cycle of the mixed layer depth averaged over 0°–30°N & 15°–65°W.

Autocorrelation in SST Observations
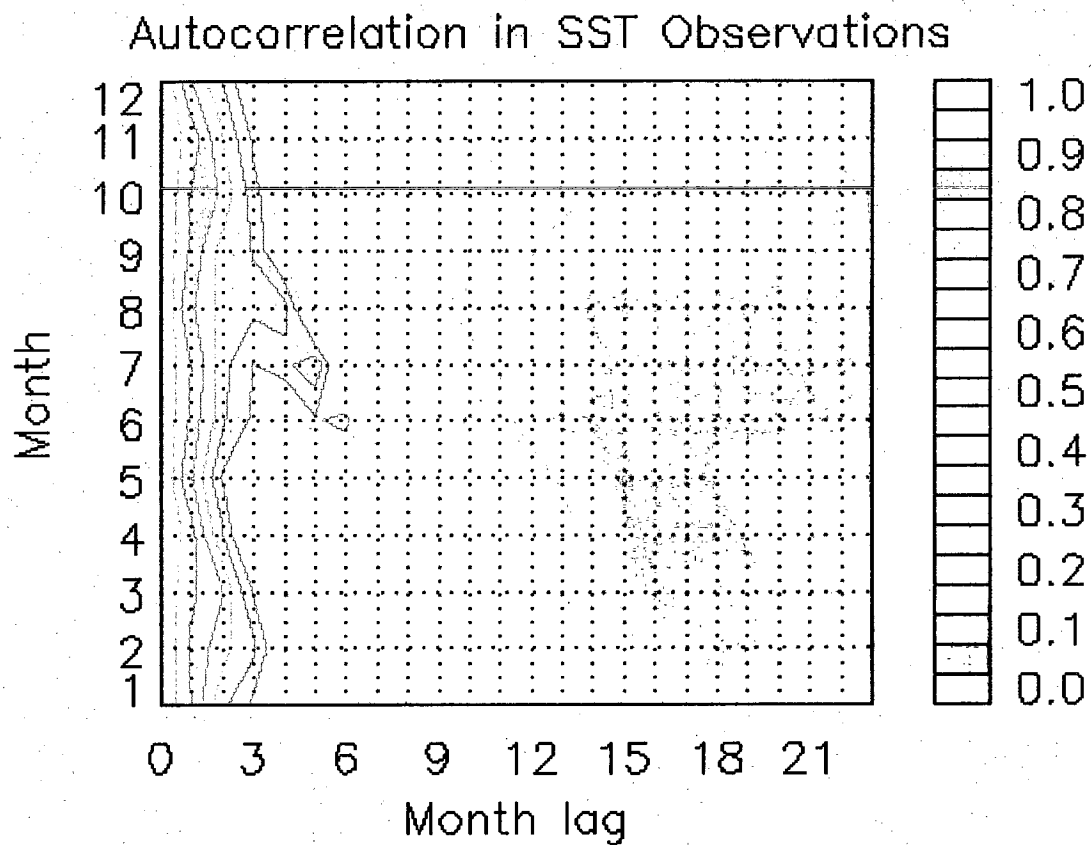
Figure 3.5 Monthly SST autocorrelation. Autocorrelation coefficients for a mean, detrended time series of SST (1955–2004), averaged over 0°–30°N & 15°–65°W.

Autocorrelation in Stochastic Model
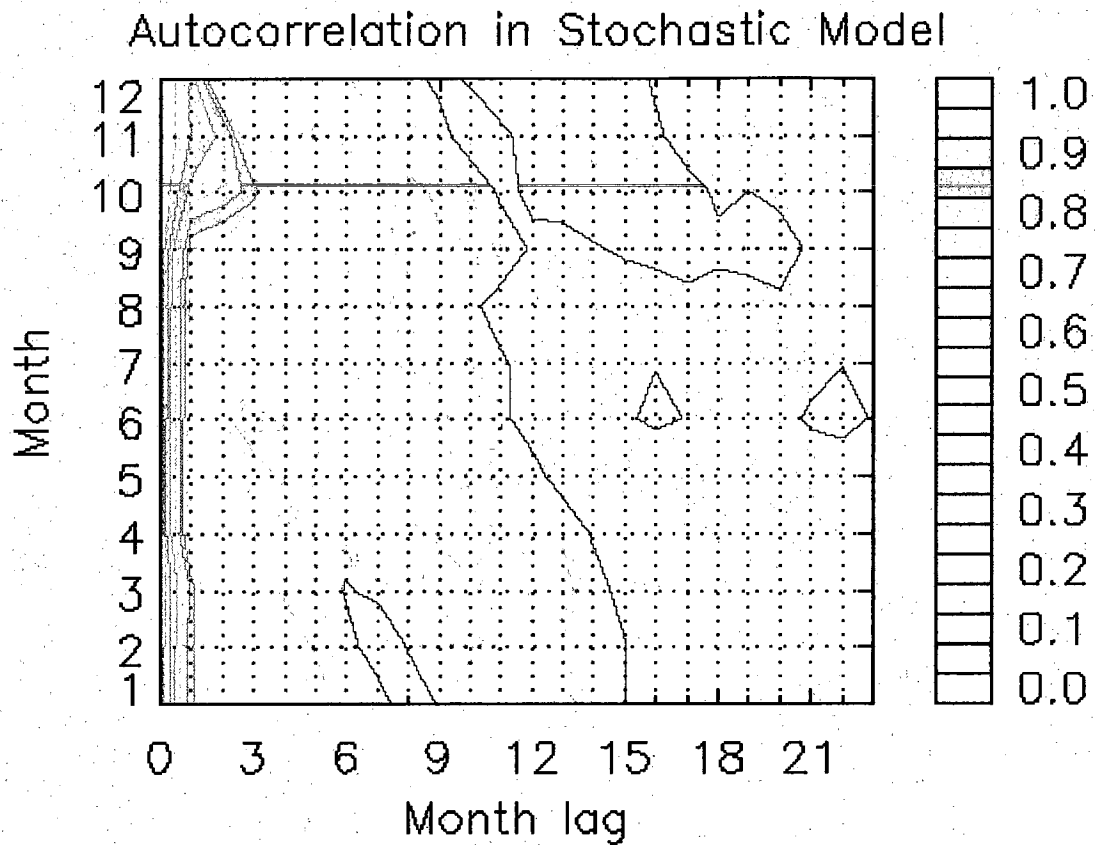
Figure 3.6 Monthly mixed layer temperatures autocorrelation from output of the stochastic model. Autocorrelation coefficients based on output from the variable mixed layer stochastic SST model after being forced for 50 years with a monthly white noise time series and averaged over the region of 0°–30°N & 15°–65°W.
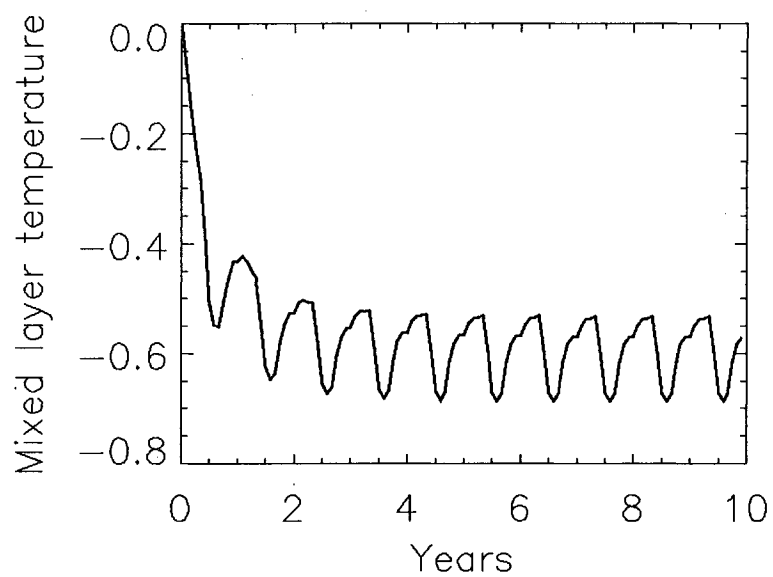
Figure 3.7 Time series of mixed layer depth temperature from model spin up. First 10 years of model output from forcing Equation 3.4, $T_{d_{seasonal}}$, with the seasonal cycle of dust surface forcing, i.e. $F' = F_{d_{seasonal}}$. Values are averaged over the region of 0°–30°N & 15°–65°W.
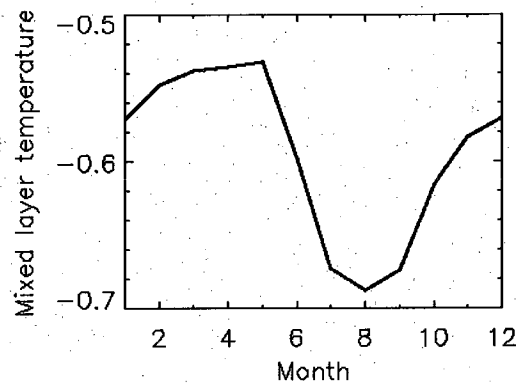
Figure 3.8 Annual cycle of mixed layer response to dust surface forcing from model spin up. Year 30 of model output from forcing Equation 3.4, $T_{d_{seasonal}}$, with the seasonal cycle of dust surface forcing, i.e. $F' = F_{d_{seasonal}}$. Values are averaged over the region of 0°–30°N & 15°–65°W.
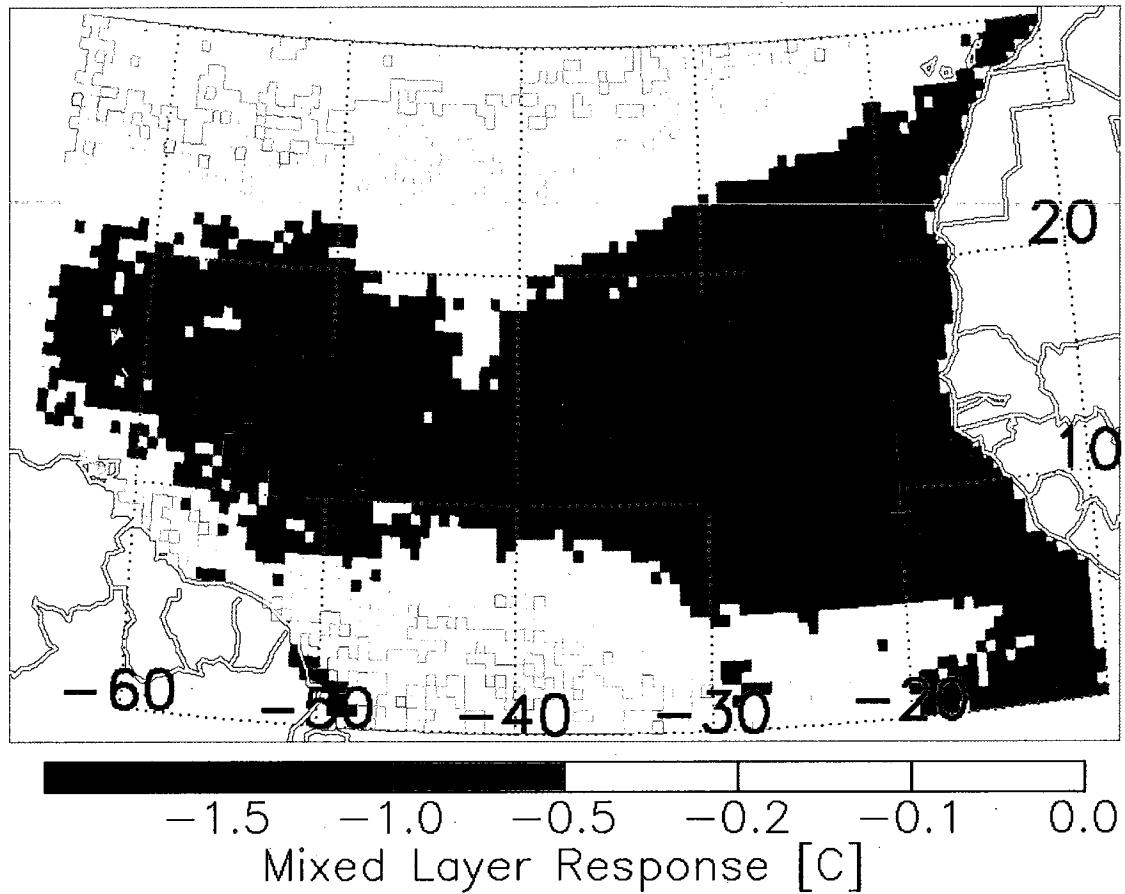
Figure 3.9 Mixed layer response to seasonal cycle of dust surface forcing. Here the temperature response of the mixed layer, $T_{d_{seasonal}}$, is the stochastic model equilibrium response to dust seasonal cycle surface forcing (i.e., the mean of year 30 from the $F' = F_{d_{seasonal}}$ model run).
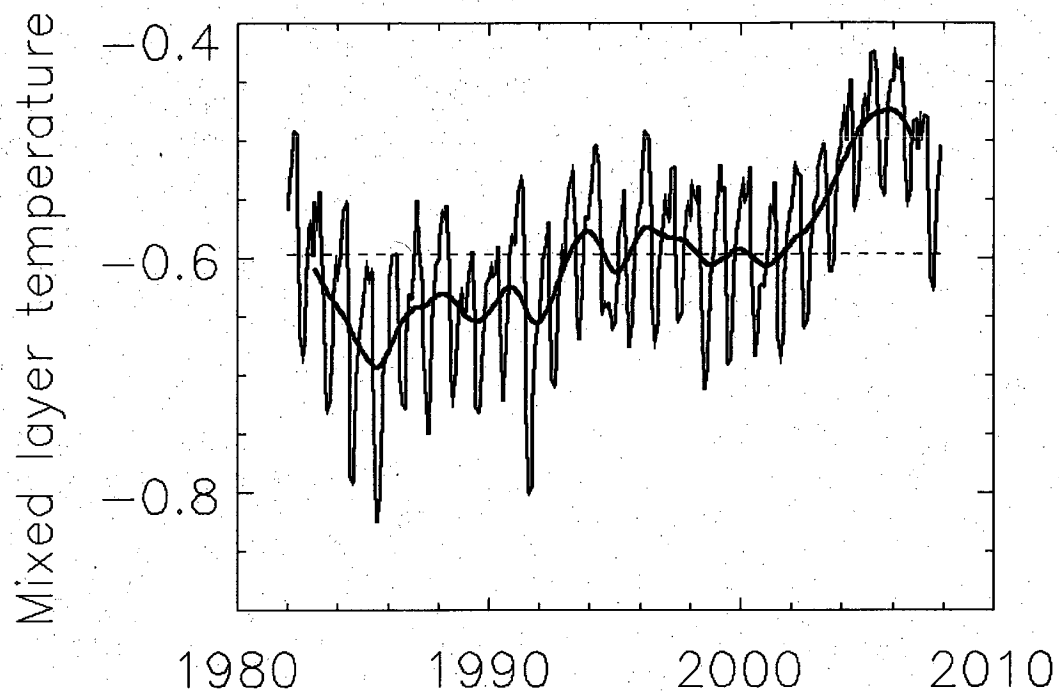
Figure 3.10 Time series of the mixed layer temperature response to surface mineral aerosol forcing. The thin black line is the monthly temperature values, the dashed line represents the series mean, and the thick black line is the monthly series smoothed with two recursive 13-month running mean filters. All series are averaged over the region of 0°–30°N & 15°–65°W.
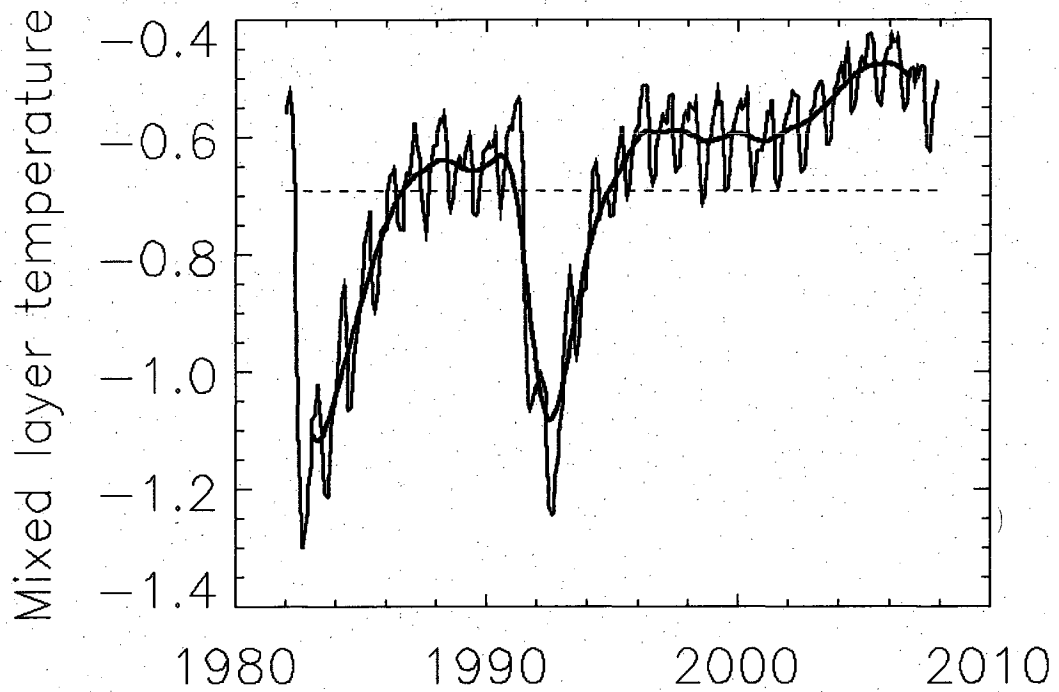
Figure 3.11 Time series of the mixed layer temperature response to surface mineral and stratospheric volcanic aerosol direct forcing. Otherwise description is the same as Figure 3.10.
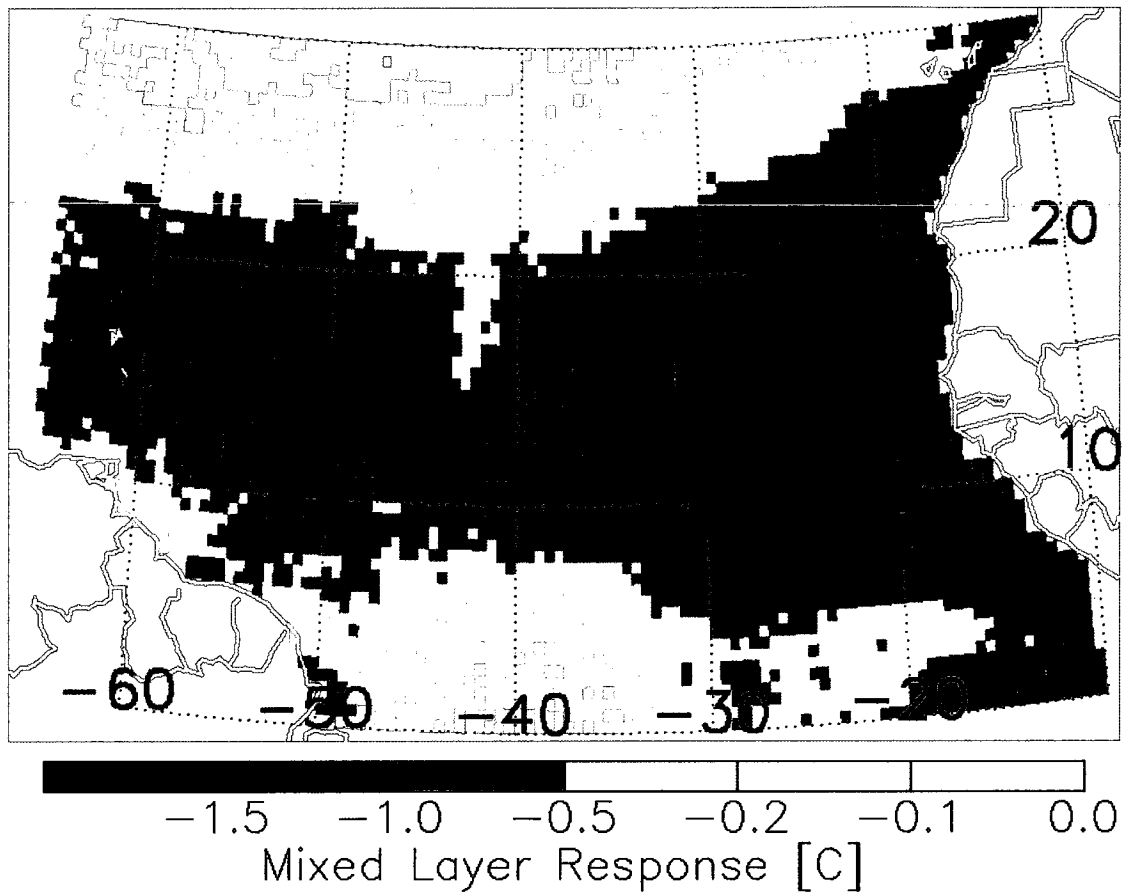
Figure 3.12 Mixed layer temperature response to dust and stratospheric aerosol surface forcing. Temperature response of the mixed layer, T_{d+s}, is the average of monthly model output over the period of 1982–2007.
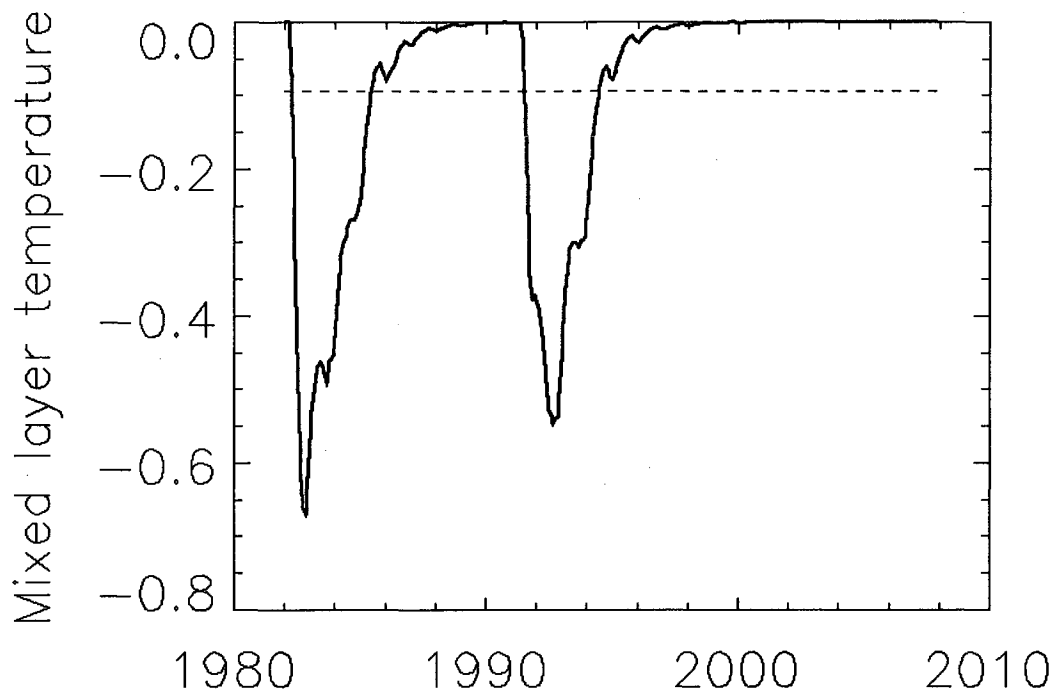
Figure 3.13 Time series of the mixed layer temperature response to stratospheric volcanic aerosol direct surface forcing. The thin black line is the monthly temperature values and the dashed line represents the series mean, both averaged over the region of 0°–30°N & 15°–65°W.
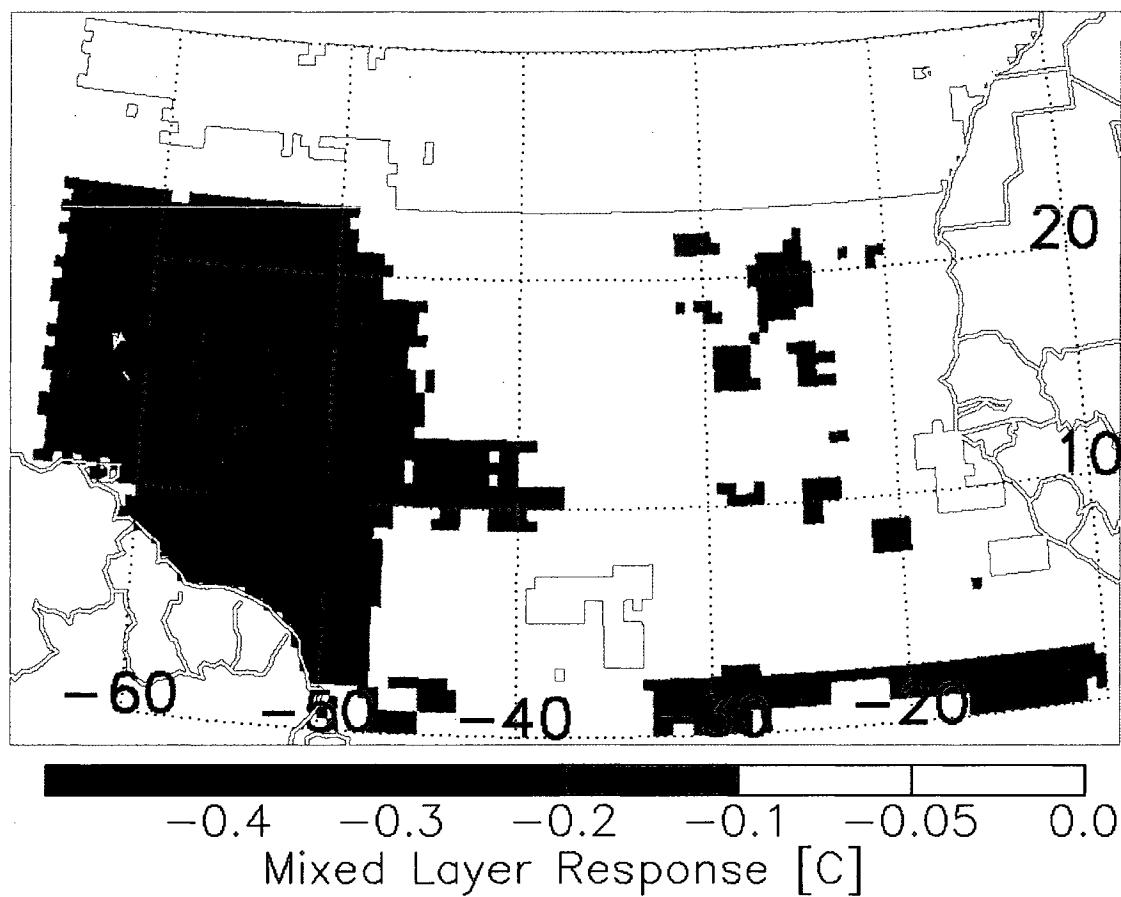
Figure 3.14 Mixed layer mixed layer temperature response to stratospheric volcanic aerosol direct surface forcing. Temperature response of the mixed layer, T_s, is the average of monthly model output over the period of 1982–2007.

4 Role of aerosols in observed sea surface temperature variability

4.1 Observed sea surface variability

Having established a methodology for estimating the mixed layer response to changes in tropospheric and stratospheric aerosols, I next consider the role of this mechanism in establishing observed sea surface temperature (SST) anomalies. To do this I use observed monthly SST from the Hadley Centre SST data set (Rayner et al. 2003)[11]. For 1982–2007 annual SST anomalies, averaged over the region of 0°–30°N & 15°–65°W, range from -0.5°C (1986) to 0.5°C (2005), with a linear trend of 0.25°C decade^{-1}, which is significant at the 99.9% level[12, 13] (Figure 4.1). The 5-year smoothed SST series shows periods of anomalous cooling and warming that are separated at 1995, a point thought to represent the transition from negative to positive phase of the Atlantic Multidecadal Oscillation (Goldenberg et al. 2001).

For the period of 1982–2007 linear trends in annual mean SST are not uniform across the tropical Atlantic basin (Figure 4.2). While all the SST trends in our region of interest and are upwards and statistically significant, they are most strongly positive (greater the 0.3°C decade^{-1}) between the latitudes of 10°-20°N and east of 50°W. It is worth noting that SST trends are not significant immediately off the coast of West Africa around 15°N (Figure 4.2), where strong upwelling may invalidate the use of this simple mixed-layer model. Although the trends in SST are statistically significant throughout the area we are interested in, the warming is most pronounced between 10°-20°N and east

---

[11] Hadley HadISST1 data is available at http://www.hadobs.org.
[12] All trends are based on the linear least squares regression of an annual mean time series onto time.
[13] All reported significance levels are based on the 2-tailed t-score for the correlation coefficients.

of 60°W, with values here exceeding 0.3°C/decade. This pattern of northern tropical Atlantic SST trends does bear resemblance to that of climatological dust loadings (Figure 2.1) and mixed layer depth (Figure 3.1).

4.2 Analysis of an "aerosol free" sea surface temperature

Since T_d is an estimate of the mixed layer response to dust surface forcing, I am able to define observed sea surface temperature as,

$$SST_o = SST_{R_d} + T_d,$$ (4.1)

where SST_o is observed SST and SST_{R_d} is the residual SST, or our estimate of SST in a "dust-free world". The magnitude of the anomalies for T_d (Figure 3.10) are about 25% of those for SST_o (Figure 4.1). Therefore, a plot of annual mean values of SST_{R_d} averaged over the region of 0°–30°N & 15°–65°W is very similar to that from the observations (Figure 4.3). However, since dust forcing was anomalously strong then weak for the first and second halves of the record, respectively, there is a 23% reduction in the upward linear trend of SST_{R_d} (0.19°C decade^{-1}) as compared to that for SST_o (0.25°C decade^{-1}).

One way to evaluate the importance of any forcing on long term SST variability is to calculate the percent change in variance between SST_o and SST_{R_d}, or the variance reduced, $R_{\sigma^2}^d$. Given Equation 4.1,

$$\sigma^2_{SST_O} = \sigma^2_{SST_{R_d}+T_d},$$ (4.2)

And therefore

$$\sigma^2_{SST_O} = \sigma^2_{SST_{R_d}} + \sigma^2_{T_d} + 2C_{SST_{R_d},T_d},$$ (4.3)

where σ_x^2 is the variance of x, and $C_{x,y}$ is the covariance of x and y. The contribution of $2C_{SST_{R_d},T_d}$ to $\sigma^2_{SST_O}$ is simultaneously attributed to both SST_{R_d} and T_d, and the relative contribution of each can not be decoupled. I therefore define

$$R^d_{\sigma^2} = 100\% \times \left(1 - \frac{\sigma^2_{SST_{R_d}}}{\sigma^2_{SST_O}}\right), \tag{4.4}$$

where $R^d_{\sigma^2}$ is the reduction in SST_O variance associated with T_d. From Equation 4.3

$$R^d_{\sigma^2} = 100\% \times \left(1 - \frac{\sigma^2_{SST_O} - \sigma^2_{T_d} - 2C_{SST_{R_d},T_d}}{\sigma^2_{SST_O}}\right), \tag{4.5}$$

which reduces to

$$R^d_{\sigma^2} = 100\% \times \left(\frac{\sigma^2_{T_d}}{\sigma^2_{SST_O}} + \frac{2C_{SST_{R_d},T_d}}{\sigma^2_{SST_O}}\right). \tag{4.6}$$

From Equation 4.6 $R^d_{\sigma^2}$ is a function of the ratio of variance in T_d and SST_O, and the covariance of SST_d and T_d, normalized by $\sigma^2_{SST_O}$. The weighted covariance term in Equation 4.6 is non-zero for the T_d, T_{d+s}, and T_s cases, solely due to the upward trends that exist in these model output time series and in SST_{R_d}. A non-zero value for this covariance term could also signify the existence of other physical processes that force ocean temperature, which are related to dust cover, e.g., aerosol indirect effects or increases in cloud cover associated with dust.

Equation 4.6 is the upper limit of the percent variance in SST_O that is driven by T_d. A lower limit on the percent variance can be estimated by setting the covariance term in Equation 4.6 to zero, which effectively assumes that all variance in this term is independent of T_d. Alternatively, by detrending both T_d and SST_O, the covariance term can be assumed to be zero. Therefore I will also report the detrended percent variance that is attributed to aerosol variability.

Similarly,

$$R^d_{\sigma^2} = 100\% \times \left(\frac{\sigma^2_{SST_{R_d}}}{\sigma^2_{SST_O}} + \frac{2C_{SST_{R_d},T_d}}{\sigma^2_{SST_O}}\right) \tag{4.7}$$

is the percent reduction in SST_O variance associated with forcing other than T_d, and represents an upper limit on the contribution by other mechanisms to SST_O variance.

$C_{SST_{R_d},T_d}$ can be expressed as

$$C_{(SST_O-T_d),T_d},\qquad(4.8)$$

allowing the definition of $R^d_{\sigma^2}$ to be expressed only as a function of T_d and SST_O,

$$R^d_{\sigma^2}=100\%\times\left(\frac{2C_{SST_O,T_d}-\sigma^2_{T_d}}{\sigma^2_{SST_O}}\right).\qquad(4.9)$$

It is important to note that our definition of $R^d_{\sigma^2}$ in Equation 4.8 is markedly different from the percent variance is SST_O explained by T_d; the square of the correlation coefficient between SST_O and T_d,

$$r^2=100\%\times\left(\frac{C_{SST_O,T_d}}{\sqrt{\sigma^2_{T_d}}\times\sqrt{\sigma^2_{SST_O}}}\right)^2.\qquad(4.10)$$

One key difference between r^2 and $R^d_{\sigma^2}$ is that r^2 is normalized by the product of the standard deviation of the two time series and is therefore invariant under linear scaling of SST_O and T_{d+s}. Equation 4.9 is normalized by the variance of SST_O, making $R^d_{\sigma^2}$ sensitive to the magnitudes of SST_O and T_{d+s}. Therefore, $R^d_{\sigma^2}$ is a more powerful metric than r^2 for understanding the relative role of T_{d+s} in shaping the variability of SST_O.

For the case of T_d Equation 4.1 $R^d_{\sigma^2}$ is 33%, and drops to 5% when the covariance term is set to zero (Table 4.1). These numbers suggest that 5-33% of the variance in SST_O can be attributed to local changes in dust cover. By repeating the analysis after detrending the smoothed time series of SST_O and T_d, $R^d_{\sigma^2}$ is equal to 7%. Therefore, mineral aerosols contribute 23% of the upward trend in northern tropical Atlantic SST and 7% of the detrended variance (Table 4.1).

While the change in the time series of northern tropical Atlantic SST for the SST_{R_d} case is modest (Figure 4.3), a map of the linear trends in SST_{R_d} shows a strong regional signal (Figure 4.4). In particular, the area of linear trends in SST_O that exceed 0.3°C decade^{-1} (Figure 4.2) now exhibits few locations where trends are greater than or equal to 0.3°C. As a whole, the trends in SST_O in regions that overlap with the areas where the mineral aerosol direct effect is non-negligible (Figure 3.9) are reduced by about 0.1°C decade^{-1}.

I next consider the case of

$$SST_o = SST_{R_s} + T_s,$$ (4.11)

where SST_{R_s} (Figure 4.5) is the residual SST after direct effects from stratospheric aerosols, T_s (Figure 3.13), are accounted for. In SST_{R_s} the magnitude of the cool anomalies from 1982 through 1995 are reduced or reverse sign (1983), except for the 1986 cool anomaly (Figure 4.5). The smoothed anomaly, from 1984–1995 is much smoother than that seen in the observations (Figure 4.1), but the impact of T_s does not extend beyond this time since forcing after 1995 is negligible (Figure 3.13). Here, $R^s_{\sigma^2}$ (the reduction in variance in SST_O via T_s) ranges from 26-53%, the reduction in the SST_O linear trend is 46%, and $R^s_{\sigma^2}$ from the detrended smoothed time series of SST_O and T_s is 55% (Table 4.1).

The map of the trends in SST_{R_s} (Figure 4.6) differs strongly from the trends in SST_O (Figure 4.2). Within our region of interest the linear trends in SST_{R_s} do not exceed 0.3°C decade^{-1}, and all values greater than 0.2°C decade^{-1} are observed east of 30°W. As is reflected in the spatial pattern of the magnitude in T_s (Figure 3.14), the trends in SST_{R_s}, relative to those in SST_O, are weaker in the western half of the basin than they are to the east. South of roughly 25°N the regions where the linear trends are greater than 0.1°C

decade^{-1} are also the areas where there are large values of DAOD (Figure 2.1), and where the trends in SST_{R_d} (Figure 4.4) are much weaker than the observations.

Lastly I examine results from

$$SST_o = SST_{R_{s+d}} + T_{s+d},$$ (4.12)

where $SST_{R_{s+d}}$ (Figure 4.5) is the residual SST after direct effects from stratospheric and tropospheric mineral aerosols, T_{s+d} (Figure 3.12), are accounted for. Maximums in temperature anomalies in the annual time series of $SST_{R_{s+d}}$ occur in 1983 and 1998 (Figure 4.5), a contrast to the SST_O series which exhibits maximums in 1998 and 2005 (Figure 4.1). Minimums in $SST_{R_{s+d}}$ are seen in 1986 and 1994, as is the case for the SST observations. The smoothed $SST_{R_{s+d}}$ series clearly shows less variance around the upward trend than is seen in any of the other anomaly temperature time series. $R^{s+d}_{\sigma^2}$ ranges from 40-76%, and after detrending the smoothed series of SST_O and T_{s+d}, $R^{s+d}_{\sigma^2}$ is equal to 67%. The upward linear trend in $SST_{R_{s+d}}$ is 0.08°C decade^{-1}, is not statistically significant, and suggests that 69% of the upward trend in SST_O can be attributed to T_{s+d} (Table 4.1).

Within the region of 0°–30°N & 10°–65°W there are no areas where the linear trends in $SST_{R_{s+d}}$ are greater than 0.3°C decade^{-1}, and there are few areas where trends are greater than 0.2°C decade^{-1} (Figure 4.6). Here, statistically significant trends in $SST_{R_{s+d}}$ are only found in the region bounded by roughly 5–10°N and 25–45°W, and north of 25°N. Throughout the rest of the area where I have estimated $SST_{R_{s+d}}$, the linear trends are between -0.2 to 0.2°C decade^{-1} and are not significant. The results shown in Figure 4.6 strongly suggest that both the strength and the spatial characteristics of the recent upward trend in northern tropical Atlantic surface temperatures are strongly dependant on local changes in aerosol cover and the resultant impact through the aerosol direct effect.

4.3 Figures
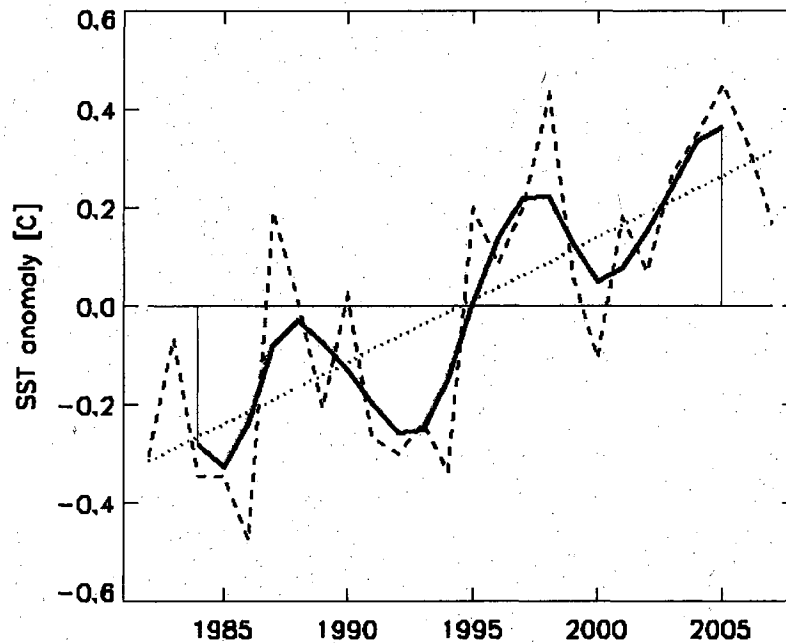
Figure 4.1 Time series of observed SST anomalies averaged over 0°-30°N & 15°-65°W. The dashed line represents the annual mean values, the thin solid line is the climatological mean, the dotted line is the linear least-squared trend, and the thick black line is the annual mean time series processed with a 1-4-6-4-1 filer, which has an e-folding reduction in the amplitude of the spectral response function for this filter at five years. The red and blue regions correspond to periods that are above and below the climatological mean, respectively.

-0.3 -0.2 -0.1 0.0 0.1 0.2 0.3

Linear Trend in SST (C/DECADE)
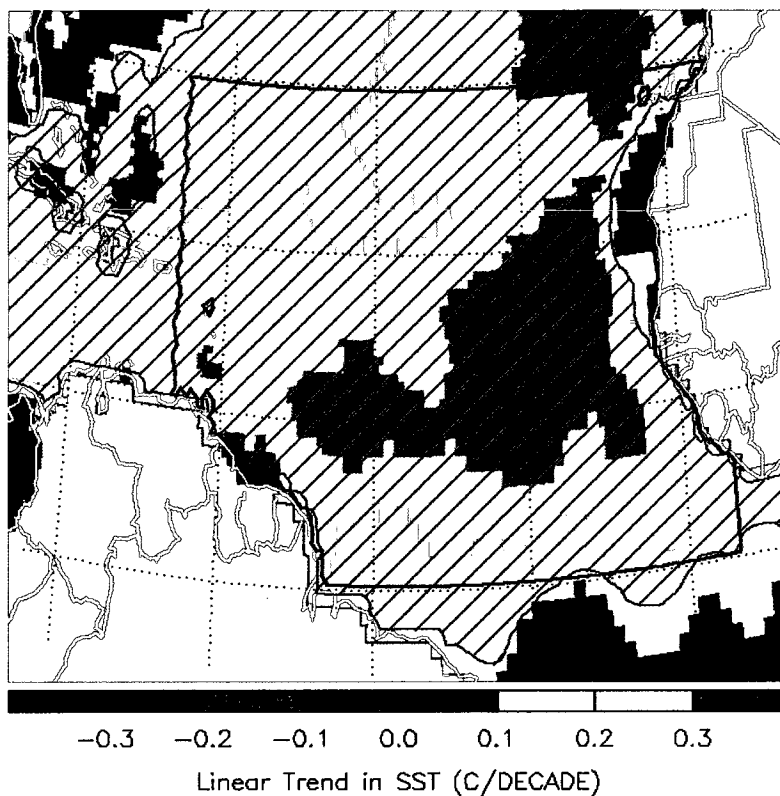
Figure 4.2 Map of linear trends in observed SST. Trends are calculated from the annual mean time series at each 0.5° grid cell over the period of 1982–2007 and are reported in units of °C decade^{-1}. Hatched areas represent regions with linear trends that are statistically significant at the 95% level. The area enclosed in the thick black lines (i.e., the oceanic regions of 0°–30°N & 15°–65°W) represents the region over which the aerosol direct effect and its impact on ocean temperatures has been estimated.
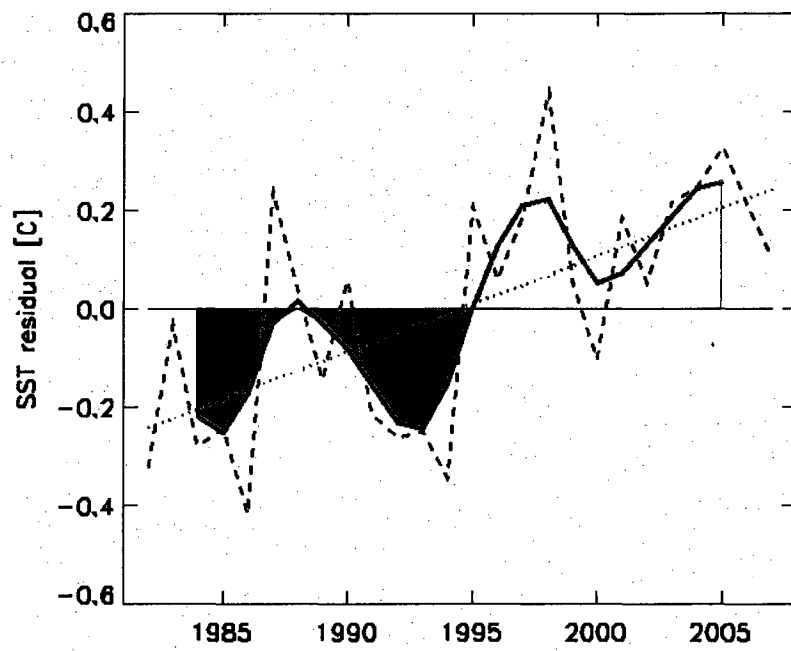
Figure 4.3 Time series of SST_{R_d}**, averaged over 0°-30°N & 15°-65°W.** Otherwise description is the same as for Figure 4.1.

−0.3   −0.2   −0.1   0.0   0.1   0.2   0.3

Linear Trend in SST (C/DECADE)
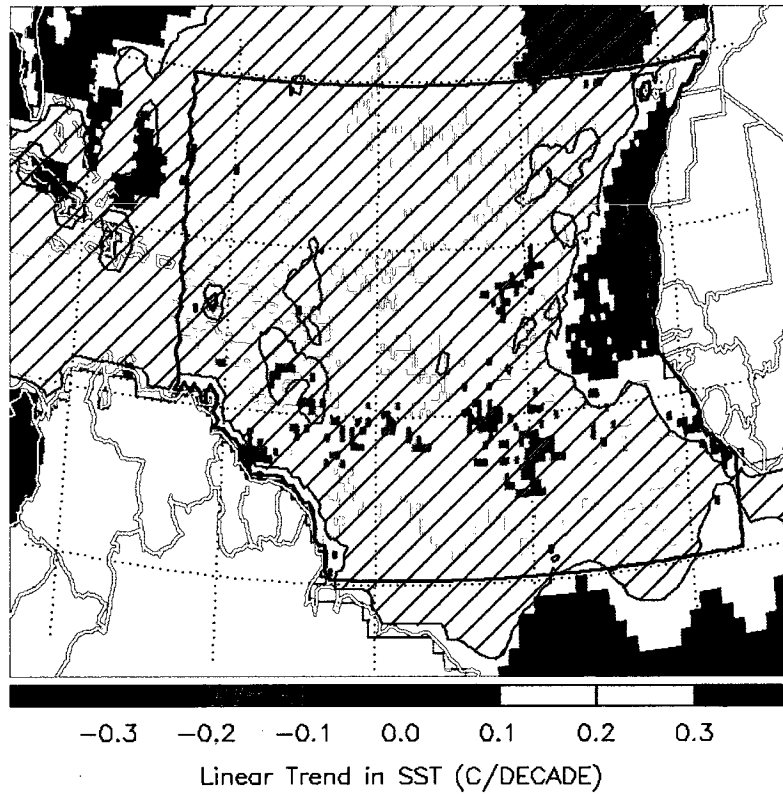
Figure 4.4 Map of linear trends in SST_{R_d}**.** Otherwise description is the same as for Figure 4.2.
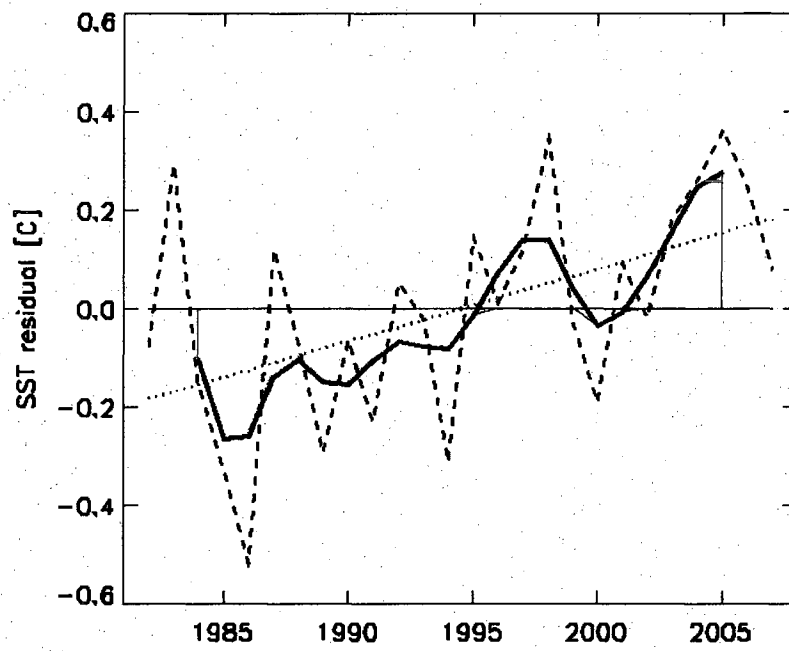
Figure 4.5 Time series of SST_{R_s}. Otherwise description is the same as for Figure 4.1.

Linear Trend in SST (C/DECADE)
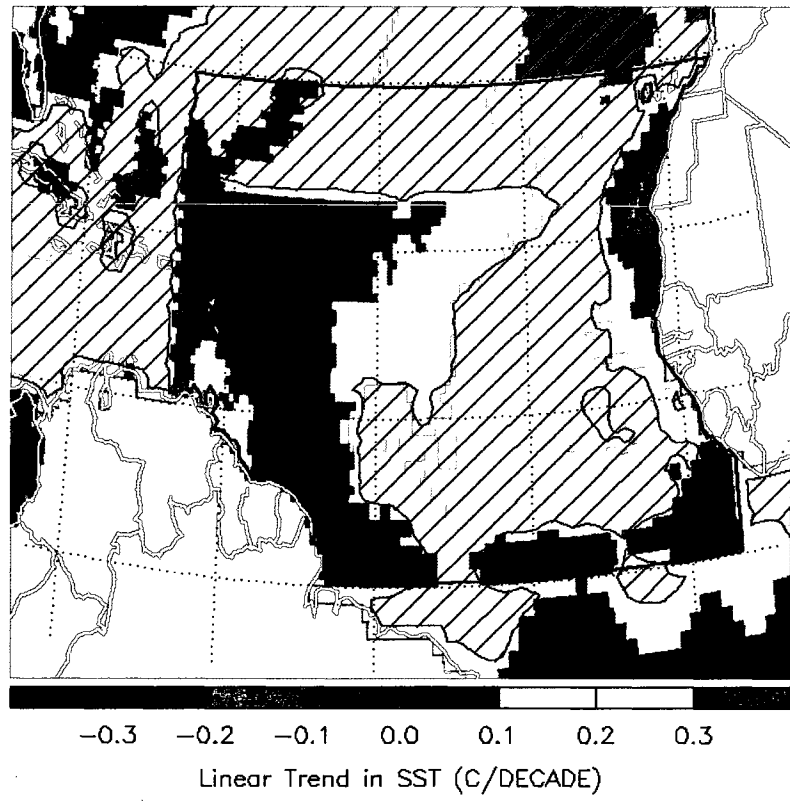
Figure 4.6 Map of linear trends in SST_{R_s}. Otherwise description is the same as for Figure 4.2.
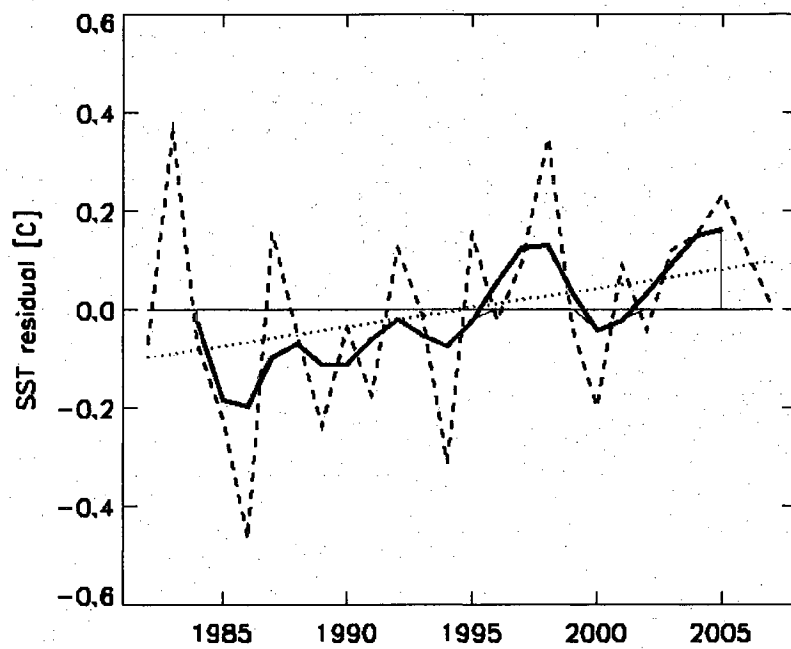
Figure 4.7 Time series of $SST_{R_{d+s}}$ **.** Otherwise description is the same as for Figure 4.1.

Linear Trend in SST (C/DECADE)
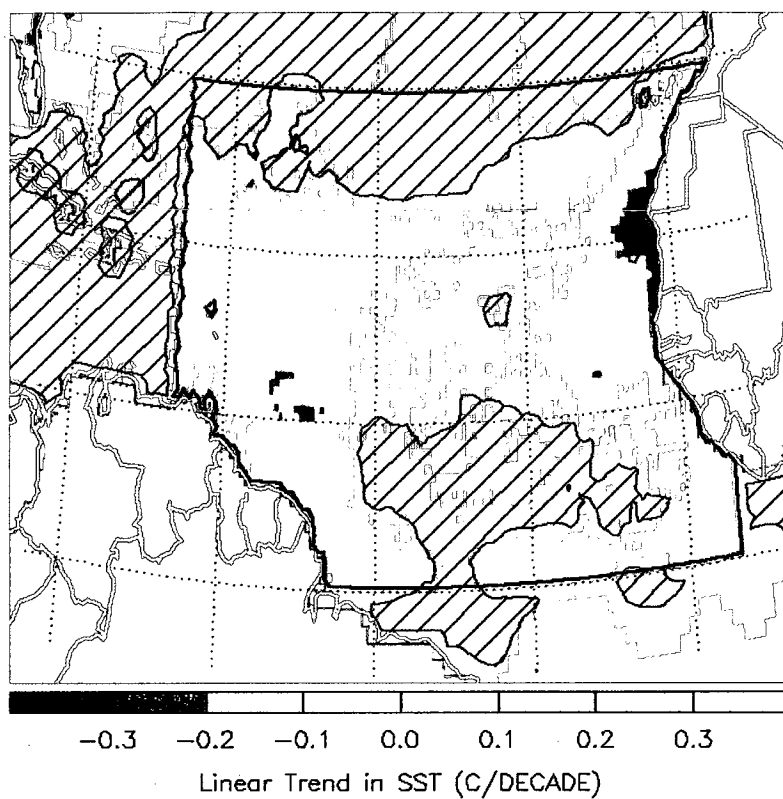
Figure 4.8 Map of linear trends in $SST_{R_{d+s}}$. Otherwise description is the same as for Figure 4.2.

4.4 Tables

	T_d	T_s	T_{d+s}
Lower limit R_{σ^2} (%)	5	26	40
Upper limit R_{σ^2} (%)	33	53	76
Detrended R_{σ^2} (%)	7	55	67
Linear trend (°C decade^{-1})	0.058	0.117	0.175
Percent of trend in SST_O.	23	46	69
Mean (°C)	-0.602250	-0.0955348	-0.697785

Table 4.1 Analysis of time series of temperature and forcing. The second and third columns represent the lower and upper limits of the percent variance in SST_O that can be attributed to the time series stated in the first row, and the fourth column gives the detrended percent variance. The fifth column is the percent of the linear trend in SST_O that can be attributed to the time series in the first row, and the last two give their linear trend values and series' means.

5 Sensitivities

Although I have demonstrated that aerosols and aerosol variability have a significant impact on observed SST anomalies across the northern tropical Atlantic, there are uncertainties associated with my methodology for estimating the impact that aerosols have on ocean temperature. By using a monthly climatological for cloudiness I am neglecting the influence of any interannual variability in cloud amount on my modeling of T_d, T_s, T_{d+s}. Therefore, keeping in mind the difficulties in using satellite observations of cloudiness in this was (as was discussed in Chapter 2), one possible solution is to utilize cloudiness estimates from the NCEP reanalysis, which are provided as monthly means with a diurnal cycle that has a 6-hour resolution. The annual time series of cloudiness from NCEP, averaged over the region of 0°-30°N & 15°-65°W shows cloudiness values ranging from about 48-54% with a mean of roughly 51% (Figure 5.1). There is some long term structure to this time series of cloudiness, with below average values in the 1980s follow by above average cloudiness for most of the 1990s, then below average cloudiness during the first half of the 2000s. The maximum in cloud cover occurs in 1996, and the minimum in 1985. Maps of mean cloud cover from ISCCP and NCEP show strong spatial differences between the two (Figure 5.2). Primary among them is the lack of a strong maximum in cloud cover over the intertropical convergence zone (ITCZ) in the NCEP data, besides the NCEP data showing lower cloud amounts throughout the basin.

Besides an increase in the mean dust forcing (Table 5.1), which results from the NCEP cloud percentages being lower than those from ISCCP, the time series of T_d when using NCEP data (Figure 5.3) differs most strongly from that when ISCCP is used (Figure 5.4) during the period of 1992–1997, where the NCEP T_d is weaker, which is due

to the increase in cloudiness during this time. There is only a small reduction in the magnitude of T_s (Table 5.2) when data from NCEP are used (Figure 5.3), but the change in T_{d+s} is compelling in that the weakening in the magnitude of the response during the mid 1990s seems to mirror similar changes in the SST anomaly during that time (Figure 5.3). This similarity is reflected in the increase in the three estimates of $R_{\sigma^2}^{s+d}$ when using the NCEP clouds (Table 4.1), over $R_{\sigma^2}^{s+d}$ when using ISCCP (Table 5.3).

In addition to exploring the model's response to different cloud data sets, to explore the sensitivities in my model I also run the radiative transfer and stochastic models with modifications to parameters that the output is strongly dependant on. This includes decreasing and increasing cloudiness by five percent, increasing and decreasing satellite retrieved aerosol optical depth by 0.1, deepening and shoaling the mixed layer depths by five meters, and using low and high estimates of the so-called feedback parameter (λ). High and low estimates of λ are made by using the 95% confidence range for the correlation coefficients for $r(\tau)$ in Equation 3.3.

With respect to T_d (Table 5.1), output from the sensitivity model runs gives ranges of 4-9% for the lower limit of $R_{\sigma^2}^d$, and ranges for the upper limit of $R_{\sigma^2}^d$ are 27-42%, while detrended $R_{\sigma^2}^d$ values go from 1-10%. The percent of the linear trend in SST_O that can be attributed to dust span 18-31%. These statistics suggest that even when the model parameters are modified enough to provide unrealistically low estimates for the dust direct effect (namely the mean of -0.21°C for the case of decreasing AOT by 0.1) local variability in dust cover has a non-negligible influence on the long term variability in observed SST anomalies.

With respect to T_s (Table 5.2), output from the sensitivity model runs gives a range of 17-45% for the lower limits of $R^s_{\sigma^2}$, and 46-76% for the upper limit of $R^s_{\sigma^2}$. Detrended $R^s_{\sigma^2}$ values are from 43-64%, and the range of estimates of the percent of the linear trend in SST_O that can be attributed to stratospheric aerosols is 37-69%. While the impact of major volcanic eruptions on surface radiation budgets is well-known, this analysis provides an observational constraints on their role in shaping SST variability.

With respect to T_{d+s} (Table 5.3), output from the sensitivity model runs gives ranges of 31-50% for the lower limits of $R^{d+s}_{\sigma^2}$, 68-85% for the upper limit of $R^{d+s}_{\sigma^2}$, and 60-71% for detrended $R^{d+s}_{\sigma^2}$. Additionally, except in the case of deepening the mixed layer depths by five meters, the linear trend in SST_R is not statistically significant in any of the sensitivity study cases (Table 5.3).

This sensitivity analysis suggests that other mechanisms that have been used to explain low frequency changes in SST, like direct effects from increases in greenhouse gasses or salinity driven changes in the thermohaline circulation, directly account for 32-15% of the low frequency SST variability over this time period (based on the upper limit of $R^{d+s}_{\sigma^2}$), and 40-29% of the detrended variance. Additionally, any other forcing on northern tropical Atlantic SST can only directly be responsible for imparting a upward trend of 0.1-0.5°C decade^{-1} on SST, or 7-39% of the observed trends in SST_O over this time period (Table 5.3). It is key to note that our analysis does not demonstrate that aerosols explain year-to-year changes in SST, but that their effect is realized when considering variability on longer time scales. This is consistent with earlier work demonstrating that interannual variability in tropical Atlantic SST is more strongly modulated by wind induced latent heat fluxes than in solar forcing (Foltz and McPhaden 2008a;Foltz and McPhaden 2006b).

5.1 Figures
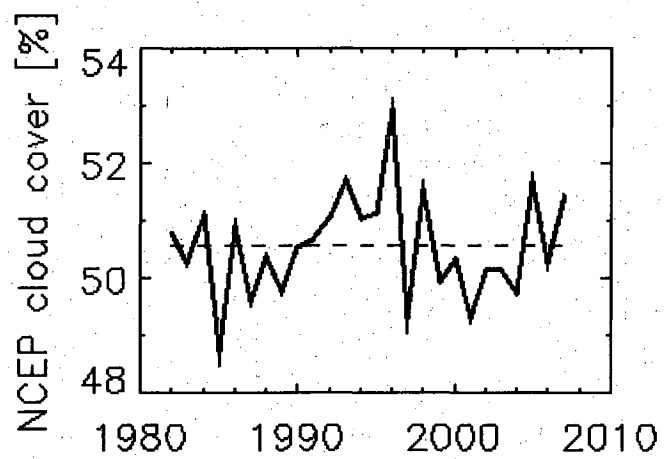
Figure 5.1 Annual time series of cloud cover from NCEP total cloud cover data, averaged over the region of 0°-30°N & 15°-65°W.
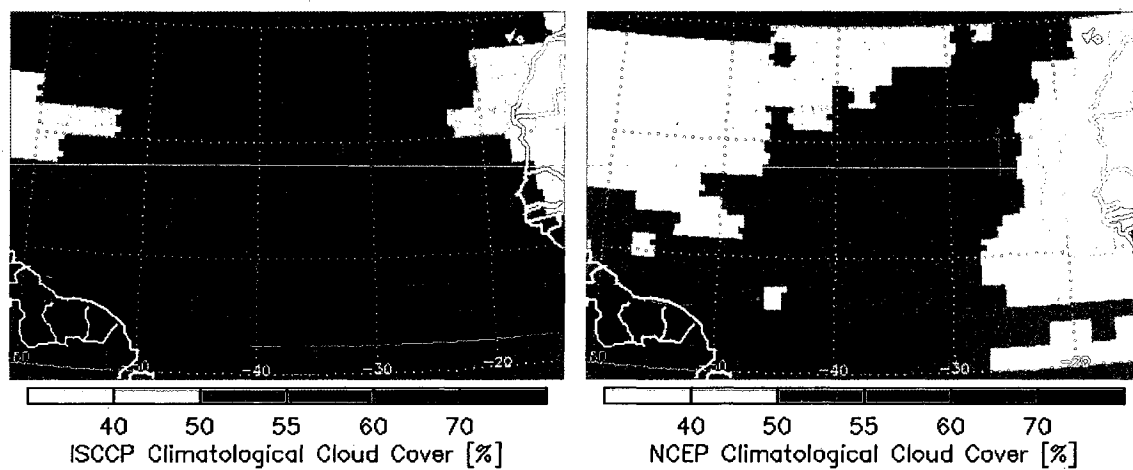
Figure 5.2 Climatological cloud cover from ISCCP (left) and NCEP (right). Both are averages of mean monthly ISCCP (NCEP) 8 (4) hourly values of total cloud cover for the period of 1984 (1982) through 2007.
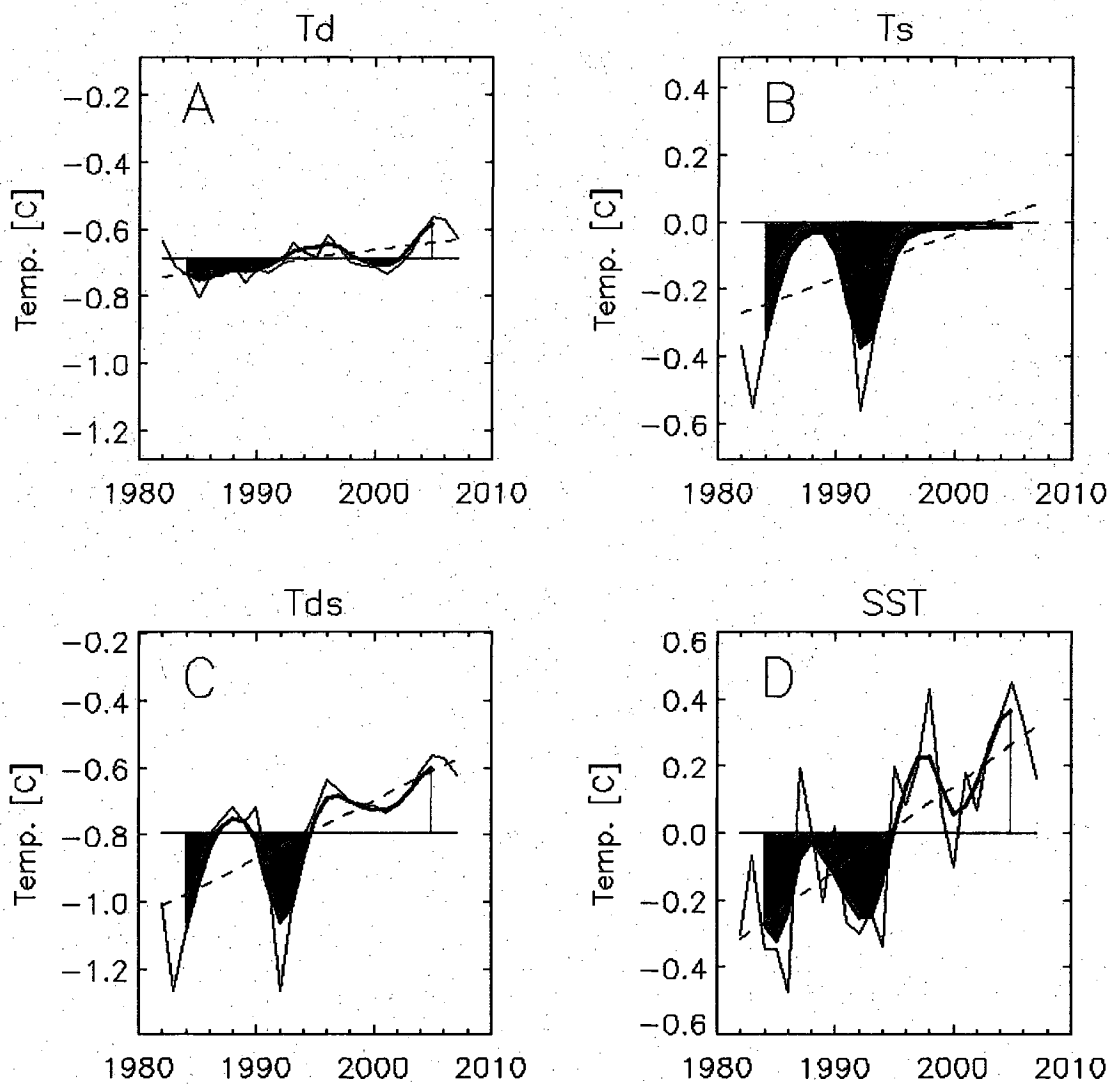
Figure 5.3 Time series of T_d, T_s, T_{d+s}, and SST_O when using cloud cover data from NCEP. In all plots the thin solid line is the annual mean time series, the thick solid line is the 5-year smoothed time series (using a 1-4-6-4-1 filter), the dashed line is the linear trend of the annual series, and red and blue regions correspond to periods of anomalously warm or cool temperatures in the smoothed series, respectively. Panels A, B, C, and D contain time series from T_d, T_s, T_{d+s}, and SST_O. Panel D is a reproduction of Figure 4.1 and included for reference. All values are averages over the region of 0°-30°N & 15°-65°W.
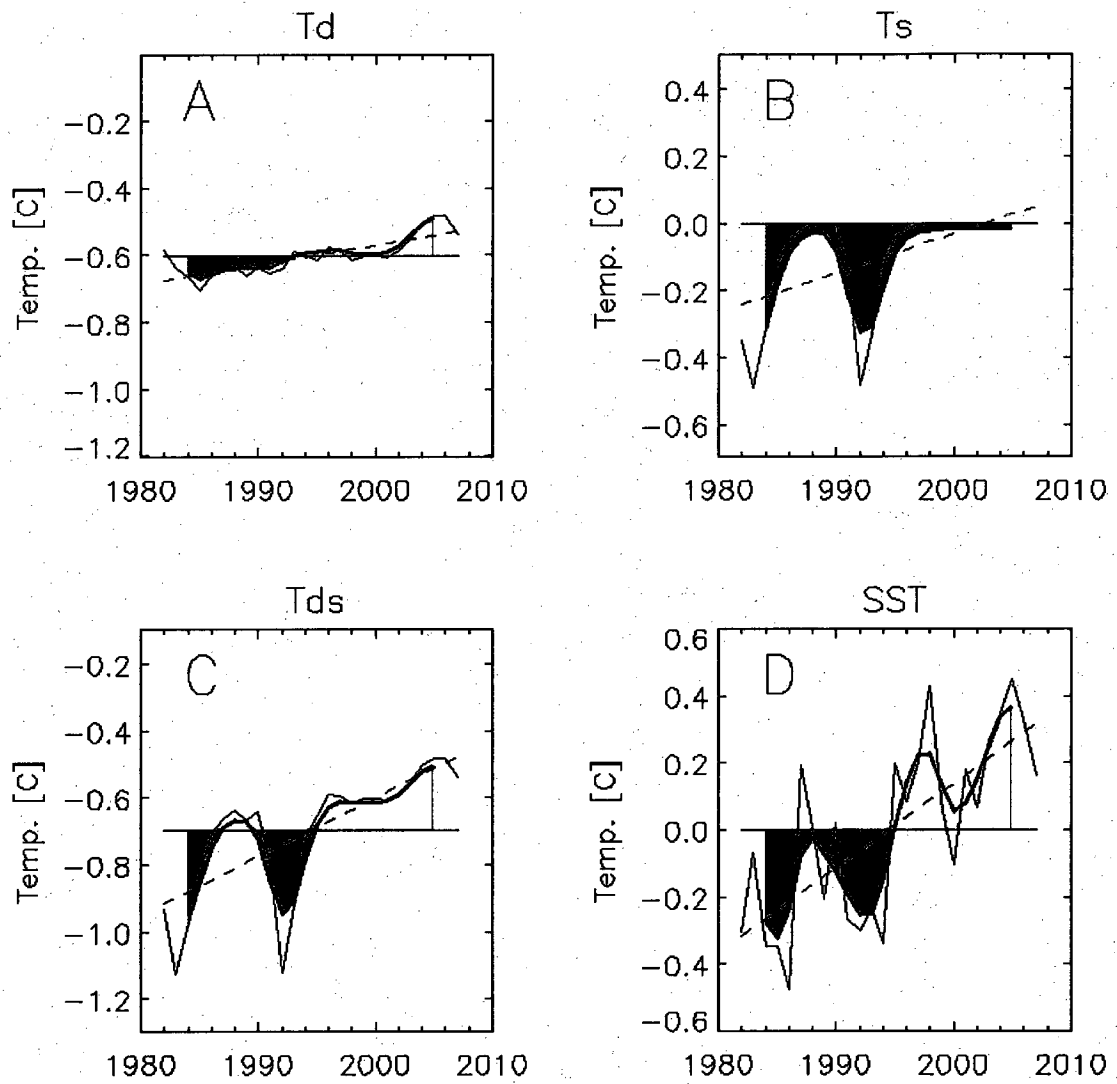
Figure 5.4 Same as for Figure 5.3 except that climatological clouds from ISCCP are used in the model.

5.2 Tables

	CF +5%	CF -5%	NCEP CF	AOT -0.1	AOT +0.1	MLD +5m	MLD -5m	high λ	low λ
Lower limit R_{σ^2} (%)	4	6	4	4	4	3	9	4	6
Upper limit R_{σ^2} (%)	30	36	25	32	31	27	42	30	36
Detrended R_{σ^2} (%)	6	7	1	5	10	6	8	6	8
Linear trend T_d (°C d^{-1})	0.05	0.06	0.05	0.05	0.05	0.05	0.08	0.05	0.06
Percent of SST_O trend.	20	26	18	21	21	19	31	21	26
Linear trend SST_R (°C d^{-1})	0.15	0.20	0.18	0.17	0.16	0.14	0.23	0.16	0.20
SST_R trend significance	99	99	99	99	99	99	99	99	99
Mean (°C)	-0.53	-0.67	-0.69	-0.21	-1.22	-0.49	-0.82	-0.54	-0.68

Table 5.1 Analysis of T_d time series. Statistics are reported for (from left to right in the first row): increasing the cloud cover by five percent, decreasing the cloud cover by 5%, using clouds from NCEP, decreasing AOT by 0.1, increasing AOT by 0.1, deepening the mixed layer by five meters, shoaling the mixed layer by five meters, using a high estimate of λ, and using a low estimate of λ. Reported statistics are (from top to bottom in the first column): lower limit of, upper limit of, detrended estimate of, linear trend in T_d, linear trend in T_d as a percentage of trend in SST_O, linear trend in SST_R, significance of linear trend in SST_R, mean value of T_d.

	CF +5%	CF -5%	NCEP CF	AOT +0.1	AOT -0.1	MLD +5m	MLD -5m	high λ	low λ
Lower limit R_{σ^2} (%)	20	32	33	41	23	17	45	21	32
Upper limit R_{σ^2} (%)	50	56	56	76	52	46	61	49	57
Detrended R_{σ^2} (%)	56	52	52	64	56	56	43	56	52
Linear trend T_s ($^{\circ}$C d^{-1})	0.10	0.13	0.13	0.17	0.11	0.09	0.16	0.11	0.13
Percent of SST_O trend.	41	52	51	69	44	37	61	42	52
Linear trend SST_R ($^{\circ}$C d^{-1})	0.20	0.19	0.21	0.13	0.20	0.21	0.17	0.20	0.19
SST_R trend significance	99	96	96	87	98	99	90	99	96
Mean ($^{\circ}$C)	-0.08	-0.11	-0.11	-0.31	-0.09	-0.08	-0.13	-0.09	-0.11

Table 5.2 Analysis of T_s time series. Otherwise description is the same as for Table 5.1.

	CF +5%	CF -5%	NCEP CF	AOT -0.1	AOT +0.1	MLD +5m	MLD -5m	high λ	low λ
Lower limit R_{σ^2} (%)	31	50	43	41	36	26	71	33	50
Upper limit R_{σ^2} (%)	72	80	77	76	74	68	85	72	81
Detrended R_{σ^2} (%)	66	66	71	64	68	65	60	66	67
Linear trend T_{d+s} (°C d^{-1})	0.15	0.20	0.18	0.17	0.16	0.14	0.23	0.16	0.20
Percent of SST_O trend.	61	77	69	69	64	56	93	63	77
Linear trend SST_R (°C d^{-1})	0.15	0.12	0.12	0.13	0.14	0.16	0.10	0.15	0.12
SST_R trend significance	94	73	86	87	92	97	27	93	74
Mean (°C)	-0.62	-0.78	-0.79	-0.31	-1.31	-0.56	-0.95	-0.62	-0.79

Table 5.3 Analysis of T_{d+s} time series. Otherwise description is the same as for Table 5.1.

6 Summary and Outlook

In this thesis I explored the role of dust outbreaks from West Africa, and long-lived stratospheric volcanic aerosols, in shaping observed northern tropical Atlantic surface temperature anomalies over the last 26 years. I first developed a method for estimating the dust component to satellite retrieved aerosol optical thickness and used this data in conjunction with independently observed stratospheric aerosol optical depth in order to create a satellite climatology of aerosol cover of the northern tropical Atlantic. I then outlined a simple model for estimating the aerosol surface forcing, using the satellite aerosol data, with two relatively simple radiative transfer models, where the shortwave model was validated against observations. These efforts resulted in the creation of a northern tropical Atlantic satellite climatology of the aerosol direct effect. I next described the model I use for estimating the ocean mixed layer response to aerosol radiative forcing at the surface. The parameters of this stochastic mixed layer model were described and I demonstrated that this simple model could reproduce observed persistence and reemergence in sea surface temperature anomalies here. I then described the output from several model runs, analyzing the spatial and temporal variability of the mixed layer response to forcing by dust, stratospheric volcanic aerosols, and both the dust and the volcanic aerosols. Following this, I analyzed the mixed layer model results in terms of observed sea surface temperature anomalies, using a simple conceptual model. From this analysis I determined that 70% of the upward trend in observed temperature anomalies is forced by aerosols, and that 65% of the low frequency variability about that trend is also forced by aerosols. Finally, I explored the sensitivity of these results to the uncertainty in various model parameters.

While this work does present compelling evidence that aerosols, via their direct effect, have a significant impact on long term northern tropical Atlantic SST variability, here I do not account for dynamical feedbacks from an atmospheric response to aerosol forcing, and the associated SST changes (Chang et al. 2000; Foltz and McPhaden 2006a; Wong et al. 2008). One possible way to explore the coupled response to the aerosol direct effect is to examine the response of an atmospheric general circulation model coupled to a slab ocean that is forced with my estimates of the aerosol surface forcing. Horizontal and vertical advection of aerosol-induced SST anomalies are also likely to be important to better quantifying the local and remote response of ocean temperature to aerosols. Therefore, efforts are now underway to force a high resolution dynamical ocean model with my estimates of the aerosol direct effect in order to explore the role of ocean dynamics in modulating the mixed layer response to aerosols, and to explore the sub surface response.

Over the last 30-years temperatures in other tropical ocean basins have been rising steadily, but at a slower rate than the Atlantic (Holland and Webster 2007). At the same time projections of surface temperature increases under a doubled carbon dioxide climate suggest that the Atlantic should be warming at a rate slower than the other observations (Vecchi and Soden 2007). I suggest this apparent disconnect between observations and models may be due to the influence of Atlantic dust cover. My results imply that since dust plays a role in modulating tropical North Atlantic Ocean temperature, projections of these temperatures under various global warming scenarios by general circulation models should account for potential long-term changes in dust loadings. This is especially critical as studies have estimated a reduction in Atlantic dust cover of 40-60% under a doubled carbon dioxide climate (Mahowald and Luo 2003), which, based on model runs

with an equivalent reduction of the mean dust forcing, could result in an additional 0.3-0.4°C warming in the tropical North Atlantic.

7 Bibliography

Barsugli, J. J., 1995: Idealized Models of Intrinsic Midlatitude Atmosphere-Ocean Interaction. Ph.D. dissertation, University of Washington, 189 pp.

Chang, P., R. Saravanan, L. Ji, and G. C. Hegerl, 2000: The Effect of Local Sea Surface Temperatures on Atmospheric Circulation over the Tropical Atlantic Sector. *J. Climate,* **13**, 2195-2216.

Darwin, C., 1846: An account of the Fine Dust which often falls on Vessels in the Atlantic Ocean. *Quarterly Journal of the Geological Society,* **2**, 26-30.

de Boyer Montégut, C., G. Madec, A. S. Fischer, A. Lazar, and D. Iudicone, 2004: Mixed layer depth over the global ocean: An examination of profile data and a profile-based climatology. *J. Geophys. Res.,* **109**, C12003.

de Graaf, M., P. Stammes, and I. Aben, 2006: Temporal and spectral variation of desert dust and biomass burning aerosol scenes from 1995–2000 using GOME. *Atmos. Chem. Phys. Discuss.,* **6**, 1321-1353.

Delany, A. C., D. W. Parkin, J. J. Griffin, E. D. Goldberg, and B. E. F. Reimann, 1967: Airborne dust collected at Barbados. *Geochim. Cosmochim. Acta,* **31**, 885-909.

Deser, C., M. A. Alexander, and M. S. Timlin, 2003: Understanding the persistence of sea surface temperature anomalies in midlatitudes. *J. Clim.,* **16**, 57-72.

Dobson, M., and J. Fothergill, 1781: An Account of the Harmattan, a Singular African Wind. By Matthew Dobson, M. D. F. R. S.; Communicated by John Fothergill, M. D. F. R. S. *Philosophical Transactions of the Royal Society of London,* **71**, 46-57.

Dobson, M., 1775: Experiments in an Heated Room. By Matthew Dobson, M. D. In a Letter to John Fothergill, M. D. F. R. S. *Philosophical Transactions (1683-1775)*, **65**, 463-469.

Dunion, J. P., and C. S. Marron, 2008: A Reexamination of the Jordan Mean Tropical Sounding Based on Awareness of the Saharan Air Layer: Results from 2002. *J. Clim.*, **21**, 5242-5253.

Ehrenberg, C. G., 1863: Erläuterung eines neuen wirklichen Passatstaubes aus dem atlantischen Dunkelmeere vom 29.Oct. 1861. *Monatsberichte der Königlichen Preuß. Akademie der Wissenschaften zu Berlin*, 202-222.

Engelstaedter, S., I. Tegen, and R. Washington, 2006: North African dust emissions and transport. *Earth-Sci. Rev.*, **79**, 73-100.

Evan, A. T., A. K. Heidinger, and M. J. Pavolonis, 2006: Development of a new over-water advanced very high resolution radiometer dust detection algorithm. *Int. J. Remote Sens.*, **27**, 3903-3924.

Evan, A. T., 2007: Comment on "How Nature Foiled the 2006 Hurricane Forecasts". *Eos Trans. AGU*, **88**, 271.

Evan, A. T. and Coauthors, , 2008: Ocean temperature forcing by aerosols across the Atlantic tropical cyclone development region. *Geochem. Geophys. Geosyst.*, **9**

Evan, A. T., A. K. Heidinger, and P. Knippertz, 2006: Analysis of winter dust activity off the coast of West Africa using a new 24-year over-water advanced very high resolution radiometer satellite dust climatology. *J. Geophys. Res.*, **111**, D12210.

Evan, A. T., A. K. Heidinger, and D. J. Vimont, 2007: Arguments against a physical long-term trend in global ISCCP cloud amounts. *Geophys. Res. Lett.*, **34**, L04701.

Feuillée, P., 1721: Osb. sur une pluie de sable dans la mer Atlantique, précédée d'une aurore boréale. *Histoire de l'Académie royale des sciences avec les mémoires de mathématique et physique,* Année 1719, L'Imprimerie Royal, 23.

Foltz, G. R., and M. J. McPhaden, 2006a: The role of oceanic heat advection in the evolution of tropical North and South Atlantic SST anomalies. *J. Climate,* **19,** 6122-6138.

Foltz, G. R., and M. J. McPhaden, 2006b: Unusually warm sea surface temperatures in the tropical North Atlantic during 2005. *Geophys. Res. Lett.,* **33**

Foltz, G. R., and M. J. McPhaden, 2008a: Impact of Saharan dust on tropical North Atlantic SST. *J. Clim.,* **21,** 5048-5060.

Foltz, G. R., and M. J. McPhaden, 2008b: Trends in Saharan dust and tropical Atlantic climate during 1980-2006. *Geophys. Res. Lett.,* **35,** L20706.

Frankignoul, C., and K. Hasselmann, 1977: Stochastic Climate Models .2. Application to Sea-Surface Temperature Anomalies and Thermocline Variability. *Tellus,* **29,** 289-305.

Game, P. M., 1964: Observations on a dustfall in the eastern Atlantic, February, 1962. *Journal of Sedimentary Research,* **34,** 355-359.

Goldenberg, S. B., C. W. Landsea, A. M. Mestas-Nunez, and W. M. Gray, 2001: The recent increase in Atlantic hurricane activity: Causes and implications. *Science,* **293,** 474-479.

Gorbushina, A. A., R. Kort, A. Schulte, D. Lazarus, B. Schnetger, H. J. Brumsack, W. J. Broughton, and J. Favet, 2007: Life in Darwin's dust: intercontinental transport and survival of microbes in the nineteenth century. *Environ Microbiol,* **9,** 2911-2922.

Hayward, J. W., 1839: Dust at Sea. Extract from the Journal of Cap. J. W. Hayward of the Brig Garland. *Naut. Mag.,* **3,** 364.

Hellman, G., 1878: Über die auf dem Atlantischen Ocean in der Höhe der Capverdischen Insehi liäiifig vorkommenden Staubfälle. *Monatsberichte der Königlichen Preussische Akademie des Wissenschaften zu Berlin.* Königliche Akademie der Wissenschaften, 364-403.

Highwood, E., J. Haywood, M. Silverstone, S. Newman, and J. Taylor, 2003: Radiative properties and direct effect of Saharan dust measured by the C-130 aircraft during Saharan Dust Experiment (SHADE): 2. Terrestrial spectrum. *J Geophys Res,* **108**

Holland, G. J., and P. J. Webster, 2007: Heightened tropical cyclone activity in the North Atlantic: natural variability or climate trend? *Philos. Trans. R. Soc. London, Ser. A,* **365**, 2695-2716.

Husar, R. B., J. M. Prospero, and L. L. Stowe, 1997: Characterization of tropospheric aerosols over the oceans with the NOAA advanced very high resolution radiometer optical thickness operational product. *J. Geophys. Res.,* **102**, 16889-16909.

Idrisi, and P. A. Jaubert, 1836: *Géographie d'Edrisi; Nuzhat al-mushtaq fi ikhtiraq al-afaq.* Vol. 5-6. Impr. royale,

Jacobowitz, H., L. L. Stowe, G. Ohring, A. Heidinger, K. Knapp, and N. R. Nalli, 2003: The Advanced Very High Resolution Radiometer Pathfinder Atmosphere (PATMOS) Climate Dataset: A Resource for Climate Research. *Bull. Am. Meteorol. Soc.,* **84**, 785-793.

James, R. B., 1838: Letter from James, R. B. (Commander Brig Spey) to Lyell, Charles, 10 March 1838.

Johnson, B. T., B. Heese, S. A. McFarlane, P. Chazette, A. Jones, and N. Bellouin, 2008a: Vertical distribution and radiative effects of mineral dust and biomass burning aerosol over West Africa during DABEX. *Journal of Geophysical Research-Atmospheres,* **113**

Johnson, B. T., S. R. Osborne, J. M. Haywood, and M. A. J. Harrison, 2008b: Aircraft measurements of biomass burning aerosol over West Africa during DABEX. *Journal of Geophysical Research-Atmospheres,* **113**

Joseph, J. H., W. J. Wiscombe, and J. A. Weinmwn, 1976: Delta-Eddington approximation for radiative flux-transfer. *J. Atmos. Sci.,* **33**, 2452-2459.

Kalnay, E. and Coauthors, , 1996: The NCEP/NCAR 40-year reanalysis project. *Bull. Am. Meteorol. Soc.,* **77**, 437-471.

Kaufman, Y. J., I. Koren, L. A. Remer, D. Rosenfeld, and Y. Rudich, 2005a: The effect of smoke, dust, and pollution aerosol on shallow cloud development over the Atlantic Ocean. *Proc. Natl. Acad. Sci. U. S. A.,* **102**, 11207-11212.

Kaufman, Y. J., I. Koren, L. A. Remer, D. Tanre, P. Ginoux, and S. Fan, 2005b: Dust transport and deposition observed from the Terra-Moderate Resolution Imaging Spectroradiometer (MODIS) spacecraft over the Atlantic ocean. *J. Geophys. Res.,* **110**, D10S12.

Key, J., and A. J. Schweiger, 1998: Tools for atmospheric radiative transfer: Streamer and FluxNet. *Computers and Geosciences,* **24**, 443-451.

Lau, W. K. M., and K. -. Kim, 2007a: How Nature Foiled the 2006 Hurricane Forecasts. *Eos Trans. AGU,* **88**, 105-107.

Lau, W. K., and K. M. Kim, 2007b: Reply to Comment on "How Nature Foiled the 2006 Hurricane Forecasts". *Eos Trans. AGU,* **88**, 271-271.

Lind, J., 1762: *An essay on the most effectual means of preserving the health of seamen, in the Royal Navy. Containing directions proper for all those who undertake long Voyages at Sea, or reside in unhealthy Situations. With cautions necessary for the Prevention of such Persons as attend the Sick in Fevers.* printed for D. Wilson, 173 pp.

Lunde, P., 1992: Pillars Of Hercules, Sea Of Darkness. *Aramco world magazine,* **43**, 6-17.

Mahowald, N. M., and C. Luo, 2003: A less dusty future? *Geophys. Res. Lett.,* **30**, 1903.

Meador, W. E., and W. R. Weaver, 1980: 2-Stream approximations to radiative-transfer in planetary atmospheres - A unified description of existing methods and a new improvement. *J. Atmos. Sci.,* **37**, 630-643.

Miller, R. L., and I. Tegen, 1998: Climate response to soil dust aerosols. *J Clim,* **11**, 3247-3267.

Miller, R. L., I. Tegen, and J. Perlwitz, 2004: Surface radiative forcing by soil dust aerosols and the hydrologic cycle. *J Geophys Res,* **109**

Moulin, C., C. E. Lambert, F. Dulac, and U. Dayan, 1997: Control of atmospheric export of dust from North Africa by the North Atlantic oscillation. *Nature,* **387**, 691-694.

Myhre, G., A. Grini, J. M. Haywood, F. Stordal, B. Chatenet, D. Tanre, J. K. Sundet, and I. S. A. Isaksen, 2003: Modeling the radiative impact of mineral dust during the Saharan Dust Experiment (SHADE) campaign. *J. Geophys. Res.,* **108**, 8579.

Norris, R., 1789: *Memoirs of the reign of Bossa Ahádee, king of Dahomy, an inland country of Guiney, to which are added the author's journey to Abomey, the capital, and a short account of the African slave trade.* Printed for W. Lowndes, 184 pp.

Preston, D. W., 1991: *The art of experimental physics.* Wiley, 432 pp.

Prospero, J. M., E. Bonatti, C. Schubert, and T. N. Carlson, 1970: Dust in the Caribbean atmosphere traced to an African dust storm. *Earth and Plan. Sci. Lett.,* **9**, 287-293.

Prospero, J. M., and P. J. Lamb, 2003: African droughts and dust transport to the Caribbean: Climate change implications. *Science,* **302**, 1024-1027.

Radczewski, O. E., 1839: Eolian deposits in marine sediments. P. D. Transk ed., Am. Assoc. Petrol. Geol., 496-502.

Rayner, N. A., D. E. Parker, E. B. Horton, C. K. Folland, L. V. Alexander, D. P. Rowell, E. C. Kent, and A. Kaplan, 2003: Global analyses of sea surface temperature, sea ice, and night marine air temperature since the late nineteenth century. *J. Geophys. Res.,* **108**, 4407.

Rossow, W. B., and R. A. Schiffer, 1999: Advances in understanding clouds from ISCCP. *Bulletin of the American Meteorological Society, Boston, MA,* **80**, 2261-2287.

Sato, M., J. E. Hansen, M. P. Mccormick, and J. B. Pollack, 1993: Stratospheric Aerosol Optical Depths, 1850-1990. *J. Geophys. Res.,* **98**, 22987-22994.

Schollaert, S. E., and J. T. Merrill, 1998: Cooler sea surface west of the Sahara Desert correlated to dust events. *Geophys. Res. Lett.,* **25**, 3529-3532.

Schotte, J. P., and J. Banks, 1780: Journal of the Weather at Senegambia, during the Prevalence of a Very Fatal Putrid Disorder, with Remarks on That Country. By J. P. Schotte, M. D.; Communicated by Joseph Banks, Esq. P. R. S. *Philosophical Transactions of the Royal Society of London,* **70**, 478-506.

Stout, J. E., A. Warren, and T. E. Gill, 2009: Publication trends in aeolian research: An analysis of the Bibliography of Aeolian Research. *Geomorphology,*

Stowe, L. L., A. M. Ignatov, and R. R. Singh, 1997: Development, validation, and potential enhancements to the second-generation operational aerosol product at the national environmental satellite, data, and information service of the national oceanic and atmospheric administration. *J. Geophys. Res.,* **102**, 16923-16934.

Stuut, J. B., M. Zabel, V. Ratmeyer, P. Helmke, E. Schefuss, G. Lavik, and R. Schneider, 2005: Provenance of present-day eolian dust collected off NW Africa. *Journal of Geophysical Research-Atmospheres,* **110**, D04202.

Tchihatchef, M. P., 1883: The Deserts of Africa and Asia. *Report of the Fifty-Second Meeting of the British Association for the Advancement of Science,* Southampton in August 1882, John Murray, 356-374.

Thomson, D. P., 1849: *Introduction to meteorology.* W. Blackwood and Son, 487 pp.

Tsay, S. C., and G. L. Stephens, 1990: A Physical/Optical Model for Atmospheric Aerosols with Application to Visibility Problems.

Vecchi, G. A., and B. J. Soden, 2007: Effect of remote sea surface temperature change on tropical cyclone potential intensity. *Nature, 450,* 1066-U9.

Ward, D., 1914: Sahara Dust over the Atlantic. *B Am Geol Soc, 46,* 49.

Wong, S., A. E. Dessler, N. M. Mahowald, P. R. Colarco, and A. da Silva, 2008: Long-term variability in Saharan dust transport and its link to North Atlantic sea surface temperature. *Geophys. Res. Lett., 35,* L07812.

Yoshioka, M., N. M. Mahowald, A. J. Conley, W. D. Collins, D. W. Fillmore, C. S. Zender, and D. B. Coleman, 2007: Impact of desert dust radiative forcing on Sahel precipitation: Relative importance of dust compared to sea surface temperature variations, vegetation changes, and greenhouse gas warming. *J. Clim., 20,* 1445-1467.